ABSTRACT

MODELING SINGLE MICROTUBULES AS A COLLOIDAL SYSTEM TO MEASURE THE HARMONIC INTERACTIONS BETWEEN TUBULIN DIMERS IN BOVINE BRAIN DERIVED VERSUS CANCER CELL DERIVED MICROTUBULES

by
Arooj Aslam

The local properties of tubulin dimers dictate the properties of the larger microtubule assembly. In order to elucidate this connection, tubulin-tubulin interactions are be modeled as harmonic interactions to map the stiffness matrix along the length of the microtubule. The strength of the interactions are measured by imaging and tracking the movement of segments along the microtubule over time, and then performing a fourier transform to extract the natural vibrational frequencies. Using this method the first ever reported experimental phonon spectrum of the microtubule is reported. This method can also be applied to other biological materials, and opens new doors for structural analysis in the life sciences.

Methods used in colloidal soft matter physics were also adapted to the study of the microtubule to develop new methods to measure local stiffness in biological materials. Using this method it is shown that there is local variability in the mechanical properties of bovine brain derived versus cancer cell derived microtubules. This provide insight to how local changes affect the dynamic instability of microtubules of different types.

Finally, a nanofluidic device to isolate single microtubules is also reported, and is designed to be used for the study of any biological polymer. It can also be adapted to incorporate nano-scale electrodes for the sensing and actuation of single isolated proteins.

MODELING SINGLE MICROTUBULES AS A COLLOIDAL SYSTEM TO MEASURE THE HARMONIC INTERACTIONS BETWEEN TUBULIN DIMERS IN BOVINE BRAIN DERIVED VERSUS CANCER CELL DERIVED MICROTUBULES

by
Arooj Aslam

A Dissertation
Submitted to the Faculty of
New Jersey Institute of Technology and
in Partial Fulfillment of the Requirements for the Degree of
Doctor of Philosophy in Materials Science and Engineering

interdisciplinary Program in Materials Science and Engineering

May 2020

APPROVAL PAGE

MODELING SINGLE MICROTUBULES AS A COLLOIDAL SYSTEM TO MEASURE THE HARMONIC INTERACTIONS BETWEEN TUBULIN DIMERS IN BOVINE BRAIN DERIVED VERSUS CANCER CELL DERIVED MICROTUBULES

Arooj Aslam

Dr. Camelia Prodan, Dissertation Advisor — Date
Associate Professor of Physics, NJIT

Dr. Gordon Thomas, Committee Member — Date
Professor of Physics, NJIT

Dr. Keun Hyuk Ahn, Committee Member — Date
Associate Professor of Physics, NJIT

Dr. Sagnik Basuray, Committee Member — Date
Assistant Professor of Chemical and Materials Engineering, NJIT

Dr. Daniel Ou-Yang, Committee Member — Date
Professor of Physics and Bioengineering, Lehigh University

Dr. Edward Bonder, Committee Member — Date
Professor of Biological Sciences, Rutgers University, Newark

BIOGRAPHICAL SKETCH

Author: Arooj Aslam

Degree: Doctor of Philosophy

Date: May 2020

Undergraduate and Graduate Education:

- Doctor of Philosophy in Materials Science and Engineering,
  New Jersey Institute of Technology, 2020
- Bachelor of Science in Electrical Engineering,
  Johns Hopkins, 2014

Major: Materials Science and Engineering

Presentations and Publications:

A. Aslam, K. Dsouza, A. Singh, E. Prodan, C. Prodan, "Using High-Speed Imaging To Measure The Vibrational Properties of Tubulin-Tubulin Interactions in Single Microtubules," *Poster Presentation*, Gordon Research Conference Motile and Contractile Systems, New London, NH, August 2017.

A. Aslam, D.J. Apigo, J. Palmieri, A. Kanwal, R. C. Farrow, E. Prodan, C. Prodan, "Microtubules: A Potential Biological Model for Topological Phonon Edge Mode Phenomena," *Invited Poster Presentation*, 61st International Conference on Electron, Ion and Photon Beam Technology and Nanofabrication, Orlando, FL, May 2017.

A. Aslam, N. Shaheen, K. Dobiszewski, A. Kanwal, R. Farrow, G. Thomas, "Observation of an Electrical Signal from a Single Molecule," *Oral Presentation*, American Physical Society March Meeting, Baltimore, MD, March 2016.

A. Aslam, A. Kanwal, G. A. Thomas, Y. Ying, Z. Iqbal, E. Farinas, R. C. Farrow, "Direct Electron Transfer From Single Enzymes to Single Wall Carbon Nanotubes," *Poster Presentation*, 59th International Conference on Electron, Ion and Photon Beam Technology and Nanofabrication, San Diego, CA, May 2015.

This Research is Dedicated to my family, from those who I grew up with, to those who I have only heard stories of. It is my family that taught me the value of education, hard work, sincerity, and honesty.

ACKNOWLEDGMENT

I want to thank Dr. Camelia Prodan and Dr. Emil Prodan for giving me the opportunity to engage a wholly new and visionary way of looking at biology. Thank you, Dr. Camelia Prodan for having the confidence in me to be a part of the team that brought the research project that was close to your heart, to fruition.

I want to thank my committee members. Dr. Keun Hyuk Ahn, thank you for being the first to hear my thesis defense, and being such a great help in such a short time frame. Dr. Edward Bonder, thank you for your insight, your thoughtful review of my thesis, and for making my defense and engaging and enjoyable experience. I am so humbled that someone actually took time to read my entire thesis, and that you actually picked out my favorite sentence! Dr. Sagnik Basuray, thank you for all your help, guidance, and collaborative spirit throughout my time at NJIT. Dr. Daniel Ou-Yang, thank you for always asking great questions that get me thinking. I hope you continue to inspire many students with your work and your mentorship. Dr. Gordon Thomas, thank you for your mentorship and guidance during all my years at NJIT.

I want to acknowledge funding support from the W. M. Keck Foundation. I also want to acknowledge technical support from the Center for Functional Nanomaterials, at the U.S. DOE Office of Science Facility at Brookhaven National Laboratory under Contract No. DE-SC0012704, and the Advanced Science Research Center NanoFabrication Facility of the Graduate Center at the City University of New York.

In particular I want to thank Dr. Farrow for his faith in me in bringing me to NJIT and onto this adventure. I want to thank Dr. Alokik Kanwal, Dr. Farrow, and Dr. Thomas for creating a lab environment that inspired innovation and welcomed any student who wanted to learn. You are all amazing teachers and mentors. I want to thank Dr. Kanwal for being one of the kindest people I know, and a most

patient teacher. He also had a superpower that got any malfunctioning equipment to magically start working just by stepping into the room, and there was never a day he wasn't smiling and laughing with everyone.

I want to thank Ssu-Ying Chen, who without I would not have survived the long hours in a dark microscope room, and the many moments of confusion and difficulty. I want to thank her for her endless positivity, her focused mind that kept us on track, her honesty, and her friendship. Ssu-Ying, I know you will change the world for the better with you sharp research mind and unwavering kindness.

I want to thank Dr. David Apigo for pushing to get things done, and being willing to go the extra mile in each project he took part in.

I want to thank my parents, Sarfraz and Rummana Aslam, and my brother, Ali Aslam, for their endless love, support, and guidance in everything I do. Their constant positivity kept me going even when things got difficult. I want to thank my mother-in-law, Rukhsana Feroz, for her encouraging words every day when I would come home from work as I worked through the last stages of my PhD.

I want to thank my husband, Qais Feroz, for his kindness and his contagious energetic spirit. His confidence in me inspired me by reminding me that hard work is always something to be proud of.

Finally, I want to thank Dr. James E. West, Dr. Reginald Farrow, and Dr. Gordon Thomas for never ceasing to inspire and encourage my young research mind, and for being fantastic role models who always have the spark of curiosity in them and inspire others to always have a love and passion for science.

TABLE OF CONTENTS

TABLE OF CONTENTS
(Continued)

Chapter **Page**

LIST OF TABLES

Table **Page**

LIST OF FIGURES

LIST OF FIGURES
(Continued)

Figure **Page**

LIST OF FIGURES
(Continued)

Figure **Page**

LIST OF FIGURES
(Continued)

Figure **Page**

CHAPTER 1

INTRODUCTION

1.1 Microtubule Role and Function

The microtubule (MT) is part of the cell skeleton. The microtubule is a tube-like assembly of smaller proteins called tubulin. The outer diameter of a microtubule is 25 nanometers, and it can grow up to hundreds of micrometers in length. The microtubule is essential in many of the cell's day to day functions. It is stiff enough to hold the shape of the cell, and can move and grow the cell in new directions. It orchestrates cell division, and aids in the active transport of nutrients across various regions of the cell.

The building blocks of a microtubule is a protein dimer made of two linked subunits, known as the alpha and beta tubulin as shown in Figure 1.1. The guanosine triphosphate (GTP) is a molecule nestled inside the protein. When tubulin docks and binds to a growing microtubule, the GTP in the β-tubulin loses a phosphate group and becomes guanosine diphosphate (GDP). The bulk of the microtubule is therefore made up of GDP-tubulin, and the ends are mainly GTP-tubulin.

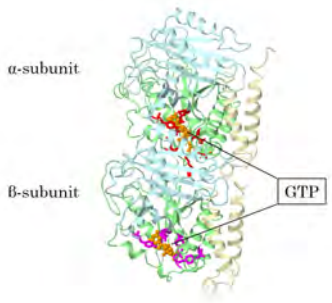

Figure 1.1 The secondary structure of a tubulin protein.[1]

The tubulin proteins bond with van der Waals forces in a repeated pattern to form the microtubule as shown in Figure 1.2. The tubulin dimers attach one on top of the other to form long chains called protofilaments, and these protofilaments then fold into the final tube-like structure. An interesting feature of the microtubule is that it is a 3-start helix. Therefore, with the typical 13-protofilament microtubule there is a mismatch when the sheet of protofilaments is rolled into a tube, resulting in a "seam" between the first and last protofilament. As the tubulin proteins self-assemble, the hydrolysis reaction of the GTP to GDP results in a conformational change in the tubulin in the bulk of the microtubule.

When the microtubule depolymerizes, or shortens, it is called 'catastrophe'. It shortens by shedding large chunks of protofilaments that curl and peel away from the microtubule. When the microtubule begins to grow again, it is called 'rescue'. This process of growing and shortening is called *dynamic instability* and is shown in Figure 1.2(e).

Dynamic instabiliy is intrinsic to the structure and pattern of the microtubule, however, surprisingly, there is no critical length or time at which catastrophe or rescue will occur. An accepted theory behind the mechanism of dynamic instability is that the GTP "cap" acts as a stabilizing factor. If GTP-tubulin in the "cap" hydrolizes fast enough that GDP-tubulin is exposed, then the microtubule falls apart. "Rescue" of the microtubule occurs when new GTP-tubulin attaches at the end of the microtubule regenerating the GTP "cap". [2]

1.2 Microtubules and the Affect of the Chemotherapy Drug Taxol

An interesting insight into microtubule dynamics comes from the effect of chemotherapy drugs on microtubules. In the 1960's the National Cancer Institute and the U.S. Department of Agriculture funded fundamental research efforts in a push to find natural treatments against cancer.[3] This resulted in the discovery of a cytotoxic

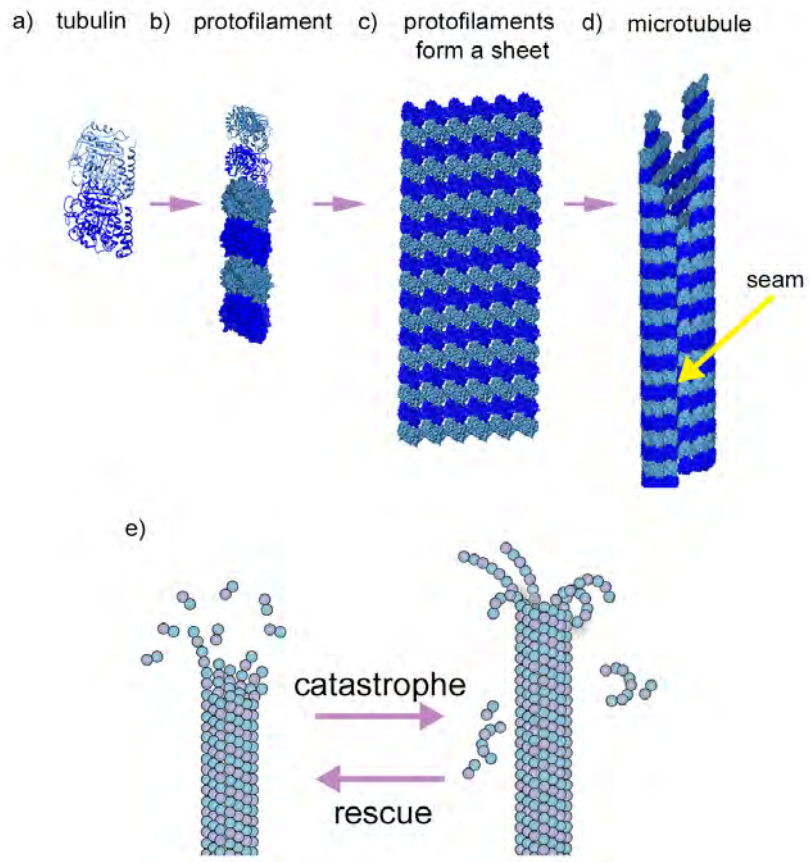

Figure 1.2 a) Tubulin protien. b) A chain of tubulin proteins called a protofilament. c) Protofilaments come together to form a sheet. d) The sheet rolls into a tube to form the microtubule. e) The depolymerization, or shortening, of a microtubule is called catastrophe. When a microtubule recovers and begins to grow againit is called rescue.

drug found in the bark of yew trees. [4, 5] This chemical, now called Taxol, can now be synthesized in a lab and is the first line of defense against breast, lung, and ovarian cancers.[6, 7] As is seen in Figure 1.3(a) Taxol disrupts dynamic instability by preventing the shortening of microtubules.[3] Taxol binds with a 1:1 stoichiometric ratio to GDP-tubulin, and it only binds to GDP-tubulin. Therefore it only binds to polymerized tubulin in the bulk of the microtubule. [8, 9, 10] When the microtubule cannot shorten, the cancer cell cannot complete cell division and the cell commits cell suicide or apopotosis. Even two to three molecules of bound Taxol every 1000 tubulin proteins can reduce the ability of microtubules to shorten.[11, 12, 13] Alushin et al. showed using cryo-EM images that the binding of Taxol reverses the conformational

change that tubulin undegoes when it hydrolyzes its GTP.[14] They propose that the bent conformation of GDP tubulin introduces strain into the microtubule bulk assembly, and the binding of Taxol releases this strain, causing there to be less stored energy avaialable for the shortening of the microtubule.[14] The success of Taxol as a chemotherapy treatment is, however, short-lived.

Cancer cells can adapt and develop a resistance to Taxol. [15, 16, 17] Even though Taxol still binds to the microtubules in the cancer cells, it no longer prevents the shortening of the microtubules.[17] One theory behind Taxol resistance is that the cell begins expressing different isotypes of tubulin.[18, 7, 19, 20, 21, 22, 23, 24, 25, 26] Tubulin proteins are classified into 7 isotypes based on changes in the C-terminal of its amino acid chain.[27, 28] Depending on which tubulin isotypes make up the microtubule, the natural shortening rates of the microtubule differ as shown in Figure 1.3(b).[11] Bovine brain tubulin is a mixture of 3% β-I, 58% β-II, 25% β-III and 13% β-IV.[29] Figure 1.3(b) shows that the natural bovine brain tubulin has the largest shortening rate. Microtubules made of only one type of tubulin isotype have shortening rates that are less than half that of the "mixed" microtubule. The affect of Taxol on the shortening rates is also different. As seen in Figure 1.3(c), β-IV tubulin microtubules need 3.6 times more bound Taxol than β-II tubulin microtubules to have a comparable change in shortening rates. Also mixed microtubules show a 93% reduction in shortening rates, whereas the β-IV microtubules have five times more bound Taxol and only show a 54% reduction in shortening rates.[11]

Typically, microtubules derived from the body contain a majority of β-I tubulin, and cancer that develops in the body is initially similarly high in β-I expression.[17, 30] Davis et al. showed that microtubules derived from the breast cancer cell line MCF-7 have 55% beta-I, 6% beta-III, 39% beta-IV and microtubules derived from HeLa cancer cell line have 90% beta-I and 10% beta-IV.[31] Cancer cells, however, have shown that they change their expression of tubulin isotypes in response to repeated

exposure to Taxol, and a majority of the increase is in the expression of β-III and β-IV tubulin.[17] The cancer cell's could be overcoming the effect of Taxol by tuning their microtubule dynamics by altering their isotype make-up.[7, 11, 32, 33, 17]

1.3 The Study of the Microtubule's Mechanical Properties

Understanding the structural properties of a microtubule is key to understanding its dynamics, and more importantly how those dynamics can be altered by changes to its structure, such as when Taxol is bound or when the isotype expression changes. The macroscopic properties of any material are a result of the collective properties of the microscopic arrangement of its building blocks. For example, carbon atoms bond together to form flat sheets of carbon that, when stacked together, create graphite. The layers of graphite easily slide past one another, making it a very useful lubricant. On the other hand, the addition of an extra bond between carbons results in a three dimensional structure that is one of the hardest materials we know, a diamond. Both materials only contain carbon, but the bonding and structure of the atoms result in drastically different macroscopic properties.

So how do we approach the study of the mechanical properties of a microtubule? Using the continuum mechanics theory, the property of the whole is defined by its building blocks. This theory breaks down a material down into small parts, defines the mechanical response of one building block, and then the building block's mechanical properties define the mechanical properties of the whole material. For example, to study the mechanics of a rigid beam, it is broken down into small length segments, dl. When the rod is in tension, compression, or bent, the deformation ϵ, or strain, of the segment dl can be measured. The relation between the stress σ (the applied force) and the resulting strain ϵ gives us what is called the Young's modulus, $E = \frac{\sigma}{\epsilon}$. The Young's modulus is a measure of the stiffness of the material, and a constant that is attributed to be a property of each segment dl. Now, knowing E, for each segment

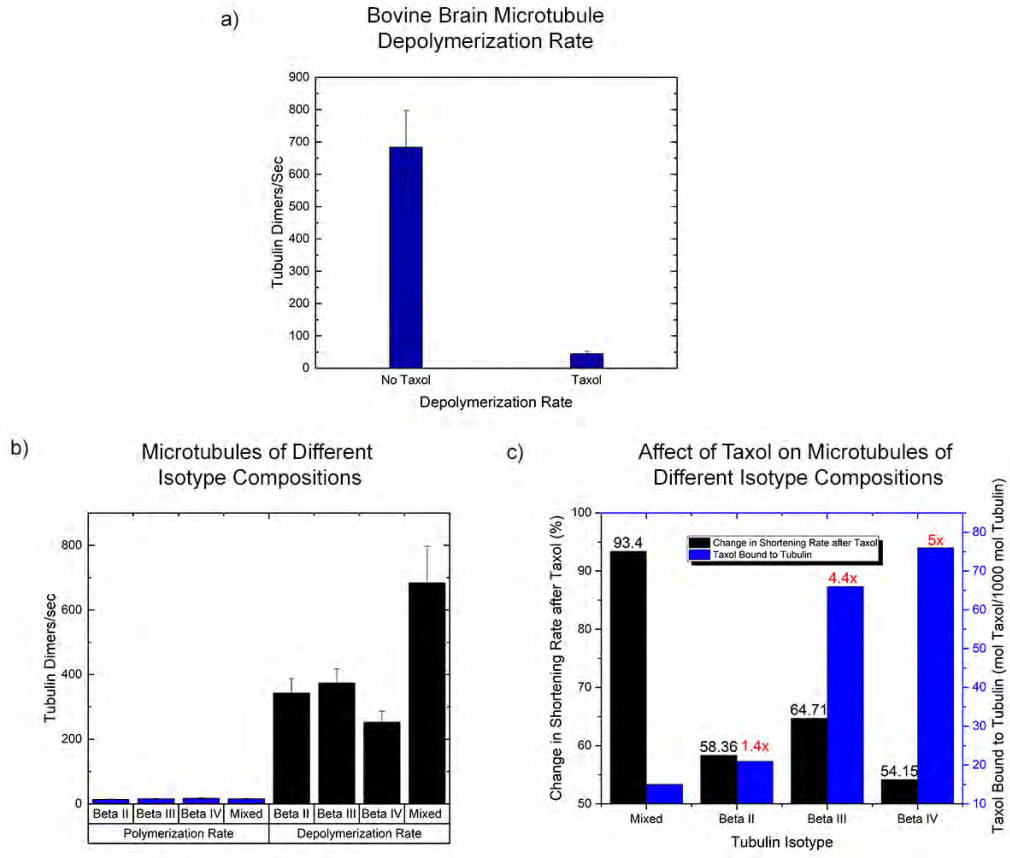

Figure 1.3 a) Bovine brain derived microtubules are measured by the number of tubulin dimers that depolymerized per second. The average shortening rates of microtubules with no Taxol bound and with 250 nM Taxol bound are shown. b)Bovine brain derived microtubules are a mixture of β-I, β-II,β-III, and β-IV tubulin, and the growing and shortening rates of bovine brain, "mixed" microtubules are compared to microtubules made up of a singe isotype. The polymerization rate is the measure of the growth of the microtubule by the number of tubulin dimers attaching per second. The similar growth rates across microtubules of different isotype compositions shows the growth rate is unaffected by the tubulin isotype. The shortening rates across microtubules of different tubulin isotype compostions show significant differences. The mixed microtubule has the fastest shortening rate and the β-IV has the slowest shortening rate. c) Taxol does not have the same affect on the shortening rates of microtubules of different isotype compositions. The left bar for each type of microtubule is the average reduction in shortening rates with the addition of Taxol. The right bar for each type of microtubule shows how much bound Taxol is needed to produce the shown reduction in shortening rates in comparison to the Taxol bound to the mixed microtubule. 250 nM of bound Taxol on the "mixed" microtubule produced a 93.4% reduction in the average shortening rate. β-II, β-III, β-IV microtubules need 1.4x, 4.4x, and 5x more bound taxol, respectively, to produce the reduction in shortening rates shown.

we can predict for any stress applied to the material how the material, a collection of interacting dl segments, will behave. In particular, the stiffness can be used to predict the resonant frequencies of the materials.

The rigid beam model has been applied to the microtubule to get a great volume of data on the Young's modulus for the microtubule using a method developed by Gittes et al. [34, 35] The Young's modulus can also be used to derive a secondary measure of stiffness called the persistence length. The persistence length is the length at which the angle of curvature of a bent beam is no longer correlated. A long persistence length means it takes a long distance for the angle of curvature to be decorrelated, which means the material is stiff. A short persistence length means the angle of curvature decorrelates in a short length scale, which means the material is flexible. The persistence lengths of a microtubule is within the .1 - 5.1 mm range, so the persistence length of a microtubule is at least an order of magnitude longer than its length making it a very stiff material.[35]

The rigid beam model, however, is simplistic in its view of the microtubule. It assumes that all the building blocks of the microtubule are the same and have the same interactions. This is untrue, and negatively impacts how we study the dynamics of the microtubule. First, the isotype composition of tubulin greatly affects the shortening rates of the microtubule, Figure 1.3(b). If we agree that microscopic structural properties dictate macroscopic behavior in materials, this change in shortening rates could be directly related to differences in structural properties between different isotypes of tubulin. Second, the microtubule is made up of GTP-bound tubulin and GDP-bound tubulin. GDP-tubulin has a bent conformation that introduces strain into the microtubule structure, and, therefore, the bulk of the microtubule has different structural properties than the ends that are composed of GTP-tubulin. Third, with Taxol-stabilized microtubules each GDP-tubulin that has Taxol bound, reverts back to a straight protein conformation, and so, in the bulk of the microtubule,

the strain is relieved in the local area where Taxol is bound creating localized differences in structural properties.

Overall, the microtubule is an anisotropic material, and minute changes in its building blocks result in drastic changes in the macroscopic dynamic behavior of the microtubule. Therefore, we need to develop structural analysis methods that can measure differences in local properties to more accurately model the anisotropic nature of the microtubule.

Furthermore, the rigid beam model as it has been applied to the structure of the microtubule is only an indirect measure of the harmonics of the microtubule. The persistence length and a Young's Modulus provides only static information about the mechanics of the microtubule. A new approach must be taken that can accurately track the microtubule's motion over time to measure the true resonant modes of the microtubule.

1.4 A New Approach to Study the Mechanical Properties of a Microtubule: The Microtubule as a Topological Material

Again and again we arrive at the question: How are local structural changes in the microtubule affecting the macroscopic property of dynamic instability? The oversimplification in how we model the structure of the microtubule has left gaps in the understanding of the mechanism of dynamic instability, which has resulted in an even larger gap in our understanding of chemotherapy drug resistance. The GTP cap theory, does not address why the GTP cap would disappear at random times, and it does not explain how a small cap of GTP can hold together microtubules of varying lengths. There is no critical length or time at which the microtubule falls apart, and how dynamic instability can be tuned by small changes in the microtubule structure is not well understood.

What can be concluded is that small changes in structure of the building blocks affects an observable change in the dynamics at the ends of the microtubule structure. So is it possible that these local changes are changing the overall energy landscape of the microtubule? Mitchison and Mahadevan proposed that microtubules are a bi-stable system with an energy minima that promotes polymerization and an energy minima that promotes depolymerization and that there is an energy barrier that must be overcome to switch between the two phases.[36] It is known that each time a tubulin protein binds to the growing microtubule, it hydrolizes a GTP and releases $12.5 kcal mol^{-}1$, and this could be a source of energy to overcome the energy barrier. However, it is unclear what perpetuates the growing phase over the catastrophe phase and vice versa, and what mechanism lies behind the transitition point. [2]

Prodan and Prodan in 2009 suggested another pathway for the microtubule to store enough energy within its strucutre that could overcome the energy barrier and cause the shortening of the microtubule. Theoretical calculations of the vibrational energies of the microtubule shows that it is possible that microtubules have an unusual phonon spectrum.[37]

Prodan and Prodan 2009 theoretically showed that the microtubule is actually a topological phononic insulator.[37] This means the structure itself forces the microtubule to have a phononic energy gap. A phononic energy gap physically means that there are a range of frequencies at which a material can be externally vibrated but no vibrations, and therefore no energy, is transferred through the material. What really makes the energy gap of a topological material unique is that there exists a singular energy state within the gap. This means that at particular frequencies within the energy gap the bulk of the material will not transfer any energy, but the edges of the material will. This energy state is called an edge mode, and each time this frequency is excited the amplitude of the vibrations at just the edges is amplified. Theoretical calculations of the vibrational energies of the microtubule show that

microtubules have edge modes that can store large amounts of vibrational energy at their tips. This could explain where the energy comes from for the transition of a growing microtubule to a shrinking microtubule.

The appearance of edge modes is completely dependent on the local interactions of the bulk material, and even small changes to the local bulk structure can shift the resonant frequency of the edge mode or completely distinguish the edge mode. Furthermore, any changes to the edges of a topological phononic insulator has no effect on the appearance of edge modes. Both of these properties of topological phononic insulators match the properties of the microtubules. The microtubule's ability to shorten, i.e. its ability to overcome the energy barrier, is greatly affected by changes in local bulk structure due to Taxol or varying tubulin isotypes. The microtubule's edge is also always changing because it is always adding new tubulin or destroying its edge during catastrophe. Therefore, it can be seen that the edge does not affect the overall dynamics of the microtubule, but the bulk structure does.

In order to discover whether or not microtubules can support edge modes, even though theoretically it has been proven that they can, the experimental phonon spectrum of a microtubule must be measured. Techniques used in solid state physics and soft matter physics can be applied to improve the study of the microtubule and bring us a step closer to uncovering the mechanism of dynamic instability. The measurement of the phonon spectrum is still a difficult task because microtubules are very stiff structures requiring high vibrational frequencies to actuate all the resonant modes. Furthermore, microtubules are not stable structures, and even though they can be made stable with the use of Taxol, they only last for a few minutes in vitro. However, nonwithstanding these challenges, steps can be taken that bring us closer to measuring the full range of resonant modes of the microtubule, and bring us closer to finding the frequency range of the energy gap. These steps are illuminated in this

dissertation, and will give us a frequency range to hone in our hunt for the theoretical edge states of the microtubule.

Islam et al. experimentally measured the density of states of a disordered colloidal crystal by measuring the small fluctuations, due to Brownian motion, of each colloid about its equilibrium. The disorder in the colloidal crystal, however, was not due to geometric imperfections in the structure, but rather was due to the inhomogeneity of the interactions between the colloids. This is very similar to the microtubule in that the assembly of the tubulin proteins is geometrically the same across microtubules, but the interactions between tubulin proteins can vary. Therefore, the model proposed by Islam et al. can be translated to the study of microtubules to extract a density of vibrational energy states and to measure of normal modes excited by thermal motion.

Islam et al. uses the concept of deriving the energy states of a Gaussian process from the covariance of observable variables of that system. In particular, he measures independent displacements of each colloid over time and constructs a matrix of their correlations, also known as the sample covariance.

$$C = \begin{Bmatrix} cov(u_1, u_1) & cov(u_1, u_2) & \dots & cov(u_1, u_N) \\ cov(u_2, u_1) & cov(u_2, u_2) & \dots & cov(u_1, u_N) \\ \vdots & \ddots & \vdots & \\ cov(u_N, u_1) & \dots & \dots & cov(u_N, u_n) \end{Bmatrix} \tag{1.1}$$

Where i and j represent the colloid position in the crystal. This matrix can be solved for its eigenvalues, which are the resonant frequencies of the system. These frequencies can then be binned into energy intervals to see the density of states of the colloidal crystal. The accuracy of the normal modes inferred from the correlations is highly dependent on the number of independent observations. Consequently, to experimentally achieve an accurate measurement, Islam et al. showed that

they needed at least 20,000 independent measurements of displacement before the eignenvalues converged.[38]

In this dissertation we present three approaches that redefine how we approach the study of the mechanics of the microtubule, and lay the foundation for experimentally measuring the density of vibrational energy states and the phonon spectrum of the microtubule. This is a key step in laying the foundation for understanding mechanical energy propagation within the microtubule structure. Chapter 3 shows how characterizing the displacement correlations of the microtubule can quantify that the interaction between tubulin dimers is harmonic in its nature. Chapter 4 shows how the standard method for measuring the Young's modulus can be generalized to go beyond just a static measure of stiffness to generate a phonon spectrum that gives a range for the acoustic resonant modes of a microtubule. Chapter 5 presents a method to use a correlation matrix of the angles along the microtubule to measure differences in the local properties between microtubules made of different isotypes. Finally, Chapter 6 shows the fabrication of a nanofluidic experimental platform for the purpose of improving our methods of introducing higher frequency external forces to the microtubule in order to actuate and measure higher resonant modes of the microtubule.

CHAPTER 2

METHODS AND MATERIALS

2.1 Methods

2.1.1 Growing Taxol Stabilized Microtubules

Pure double-cycled tubulin and tubulin labeled with Alexa488 and Alexa594 were stored at -80 C in PEM buffer (80 mM piperazine-N,N'-bis2-ethanesulfonic acid (PIPES), 1 mM ethylene glycol tetraacetic acid (EGTA), 1mM $MgCl_2$, pH 6.9).

To grow stabilized microtubules the tubulin was thawed on ice and grown in a GPEM buffer (1 mM guanonine triphosphate (GTP), 80 mM PIPES, 1 mM EGTA, 1mM $MgCl_2$, pH 6.9) with 10% dimethyl sulfoxide (DMSO). The solution was incubated on ice for 5 minutes and then incubated at 37 C for one hour. The tubulin was grown at 2 mg/ml with 10% to 50% labeled tubulin. After incubation, warm Taxol was added to a final concentration of 10 μM. The stabilized microtubules were diluted 100 times in an anti-bleaching solution (250 nM glucose oxidase, 64 nM catalase, 40 mM D-glucose, 1% beta-mercaptethanol (BME)) before imaging. [39]

Samples for imaging were prepared by coating the glass slide and coverslip with bovine serum albumin (BSA), dropping 1.5 - 2 μl of the diluted microtubule solution onto the slide, and sealing the coverslip to the slide with 1-minute epoxy.

2.1.2 Growing Segmented Microtubules

Pure double-cycled tubulin and tubulin labeled with Alexa488 and Alexa594 were stored in -80 C in PEM buffer (80 mM piperazine-N,N'-bis2-ethanesulfonic acid (PIPES), 1 mM ethylene glycol tetraacetic acid (EGTA), 1mM $MgCl_2$, pH 6.9). MCF-7 breast cancer cell derived tubulin and HeLa cancer cell derived tubulin was purchased from Cytoskeleton, Inc. and stored in -80 C in PEM buffer (80 mM

piperazine-N,N'-bis2-ethanesulfonic acid (PIPES), 1 mM ethylene glycol tetraacetic acid (EGTA), 1mM $MgCl_2$, pH 6.9).

To grow segemented microtubules the tubulin was thawed on ice and the microtubules are grown in a GPEM buffer (1 mM guanonine triphosphate (GTP), 80 mM PIPES, 1 mM EGTA, 1mM $MgCl_2$, pH 6.9) with 10% dimethyl sulfoxide (DMSO). The solution was incubated on ice for 5 minutes and then incubated at 37 C for one hour. The tubulin was grown at 2 mg/ml cancer cell derived tubulin with 10% labeled bovine brain tubulin. The bovine brain tubulin and cancer cell derived tubulin solutions were put into a vial one after the other without mixing. This promotes the nucleating and growing of tubulins concentrated into cancer cell derived and bovine brain derived tubulin segments. After incubation, warm Taxol was added to a final concentration of 10 μM. The stabilized microtubules were diluted 100 times in an anti-bleaching solution (250 nM glucose oxidase, 64 nM catalase, 40 mM D-glucose, 1% beta-mercaptethanol (BME)) before imaging. [39]

Samples for imaging were prepared by coating the glass slide and coverslip with bovine serum albumin (BSA), dropping 1.5 - 2 μl of the diluted microtubule solution onto the slide, and sealing the coverslip to the slide with 1-minute epoxy.

2.1.3 Imaging and Tracking Microtubules

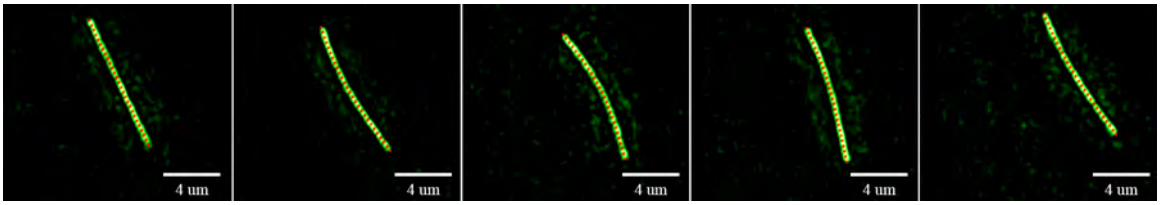

Figure 2.1 Tracking of microtubule (green) segmented into 26 blocks. Each point (red) represents the position of the center of mass of that block.

A Prime 95B^{TM} Scientific CMOS Camera was used to acquire videos of the microtubules at 10-100 frames per second.

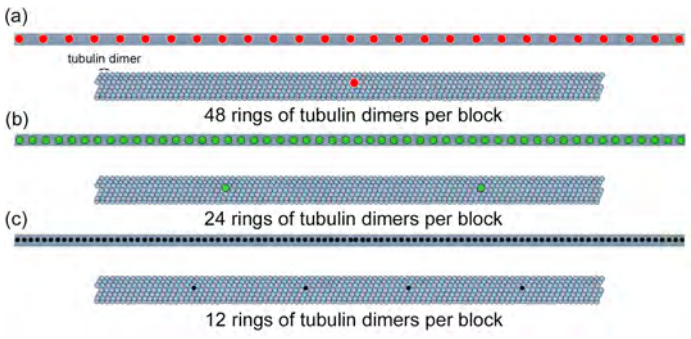

Figure 2.2 The points along the microtubule represent the center of mass of each block. (a) A microtubule segmented into 26 blocks with a point representing the position of center of mass. (b) A microtubule with 50 blocks. (c) A microtubule with 100 blocks.

The plug-in JFilament in FIJI was used to find the initial coordinates of the microtubule.[40] The ends of the microtubule can easily move out of focus, and this results in missing data points in the tracking. Therefore, only microtubules that stayed in focus for 1000 frames with a standard RMS deviation in length of less than 1% were used for analysis to ensure that the length of the tracked microtubule did not change significantly over time.

The coordinates from JFilament were then fit to a spline in MATLAB, and segmented into 26, 50, or 100 equal length blocks. Each block is represented by the position of its center of mass as shown in Figure 2.2.

2.1.4 Measuring Persistence Length Using a Bootstrapping Method

The flexural rigidity and persistence length were measured by approximating the microtubule's curvature, $\theta(s)$, as a Fourier cosine series where $\theta(s)$ is the angle of each block to the horizontal, s is the block length, and L is the total length of the microtubule [34]:

$$\theta(s) = \sqrt{\frac{2}{L}} \sum_{q=0}^{\infty} a_q \cos\left(\frac{q\pi s}{L}\right) \tag{2.1}$$

The microtubule's potential energy, U, is then modeled as the bending potential energy of a rigid rod, where EI is the flexural rigidity.

$$U = \frac{1}{2} EI \int_0^L (d\theta/ds - d\theta^0/ds)^2 ds \tag{2.2}$$

Combining Equation (2.1) and (2.2), the bending potential energy becomes:

$$U = \frac{1}{2} EI \sum_{q=0}^{N-1} \left(\frac{q\pi}{L}\right)^2 (a_q - a_q^0)^2 \tag{2.3}$$

Where N is the number of positions tracked along the microtubule. Each term from Equation (2.3) contributes with an average $\frac{1}{2}k_bT$, according to the equipartition theorem. This implies that:

$$\frac{k_bT}{EI}\left(\frac{L}{q\pi}\right)^2 = \langle (a_q(t+\Delta t) - a_q(t))^2 \rangle_{t,\Delta t>\tau} = \mathrm{var}(a_q) \tag{2.4}$$

The persistence length is defined as $L_p = \frac{EI}{k_bT}$, Equation (2.4), therefore:

$$\mathrm{var}(a_q) = \frac{1}{L_p}\left(\frac{L}{q\pi}\right)^2 \tag{2.5}$$

Equation (2.5) shows that one can obtain the persistence length of a polymer by measuring the variance over time of the Fourier coefficients, as long as the modes are uncorrelated.

Accounting for the noise term due to the resolution of the microscope and camera, Equation (2.5) becomes:

$$\mathrm{var}(a_q) = \left(\frac{L}{q\pi}\right)^2 \frac{1}{L_p} + \frac{4}{L}\langle \epsilon_k^2 \rangle \left[1 + (N-1)\sin^2\left(\frac{q\pi}{2N}\right)\right] \tag{2.6}$$

where ϵ_k is a fitting parameter that accounts for the experimental error.[34]

The first few modes are prone to oversampling because of the frame rate of the video. To remove bias in the variance measurement due to oversampling, an autocorrelation function was used on the variance of the first mode to determine a correlation time, τ.[35] The correlation time was then used to find the number of time independent frames in the data set, $N_{ind} = \frac{Total\,Number\,of\,Frames}{\tau}$. N_{ind} frames were then selected randomly and the variance was solved using Equation (2.4). This was repeated 5000 times with replacement using a bootstrapping method coded in R to get a standard deviation for the variance of each Fourier coefficient. The variance of the Fourier coefficients was plotted against the mode number. Finally, multiple linear regression fitting was used to solve Equation (2.6) for L_p and ϵ_k.[35]

The average length of the microtubule over all frames was used in all calculations. There are small changes in length as the fluorescence intensity changes slightly for each frame because the ends and the microtubule fluorescence bleaches over time. Only microtubules that had a standard RMS deviation in length of less than 1% were used for analysis.

Table 2.1

Material Name	Storage and Stock Concentrations	Vendor
Double Cycled Unlabeled Tubulin	-80 C 20mg/ml	PurSolutions Cat# 032005
Double Cycled Labeled Tubulin	-80 C 2mg/ml in PEM Buffer	PurSolutions Cat# 059405 Cat# 048805
Beta-D-Glucose	-20 C 2mg/ml in PEM buffer	Fisher Scientific Cat# 492-61-5
Beta-mercaptethanol	4 C 10 uL aliquots	Fisher Scientific Cat# O3446I-100
Bovine Serum Albumin (BSA)	-20 C 20mg/ml	Fisher Scientific Cat# BP9703100
Catalase	4 C	Fisher Scientific Cat# ICN10042910
Dimethyl Sulfoxide	Room Temperature	Fisher Scientific Cat# 67-68-5
Ethylene glycol tetraacetic acid (EGTA)	Room Temperature	Fisher Scientific Cat# 60-018-20
Glucose Oxidase	-20 C 2mM in PEM buffer	Fisher Scientific Cat# 34-538-610KU
Guanonine Triphosphate	-20 C 10mM in PEM buffer	Cytoskeleton Inc. Cat# BST06-010
Paclitaxel (Taxol)	-20 C 1mM in DMSO	Cytoskeleton Inc. Cat# TXD01
Piperazine-N,N'-bis2-ethanesulfonic acid (PIPES)	Room Temperature	Sigma Aldrich Cat# P6757
Magnesium Chloride (MgCl)	Room Temperature	Fisher Scientific Cat# M33-500

CHAPTER 3

HARMONIC INTERACTIONS ARE THE UNDERLYING MECHANICS OF A MICROTUBULE: STATISTICAL MODEL OF A MICROTUBULE

3.1 Introduction

The models used to study the microtubule in both experiement and simulation utilize the assumption that the tubulin proteins interact like a harmonic oscillator and can be modeled by the potential energy function:

$$U = \frac{1}{2}kx^2 \tag{3.1}$$

This assumption is to simplify the calculations of a complex system like a microtubule, and it has been very useful in modeling the microtubule.[41, 34, 35] However, in order to move towards measuring the dynamic mechanics of the microtubule and to be able to say that we can map the local differences in stiffness along the microtubule, this assumption needs to be tested. If the assumption of a harmonic potential is true, then we can confidently take one more step towards modeling the harmonics of the microtubule. We have experimentally shown that tubulin proteins do indeed follow the rules of a harmonic oscillator.

3.2 The Configuration Space of the Microtubule Lattice

Configuration space is defined by the parameters we use to characterize our system. In a microtubule each tubulin dimer can occupy a certain position in space, and if there are N tubulin dimers then, due to our configuration space, our system (the mictotubule) has x^N possible states, where x represents the position. The configuration space of a microtubule is very large if each protein is considered. However, the microtubule can be segmented such that we can deal with a reasonable

configuration space upon which we can derive both mesoscale and microscale data to lead to a more locally defined vibration analysis model.

3.3 Analysis of the Macroscopic Degrees of Freedom

This section is dedicated to the analysis of the macroscopic degrees of freedom. The degrees of freedom are the independent parameters that define a system. For a true macroscopic system, these parameters will be fixed, but for MTs we can measure macroscale degrees of freedom in order to then decouple them from the microscopic degrees of freedom.

Figure 3.1(a) illustrates the configuration of a microtubule tracked using the methods in Chapter 2. The number of the beads will be denoted by N_B and their positions by $\boldsymbol{r}_j = (x_j, y_j)$. Also, the number of frames in a recording will be denoted by N_F. The microtubules are recorded using a microscope with a fixed field of view, and the positions are referenced with respect to the field of view in this configuration. The segmented blocks that represent the microtubule are characterized by macroscopic degrees of freedom used to determine the center of mass and the orientation of the microtubule.

3.3.1 Length Analysis

The MTs selected for our study are confined in the two-dimensional focal plane of the microscope, and heavily stablized with Taxol that prevents them from depolymerizing and keeps the length constant during imaging. The length of the microtubule is measured by:

$$L = \sum_{j=1}^{N_B-1} |\boldsymbol{r}_{j+1} - \boldsymbol{r}_j|. \tag{3.2}$$

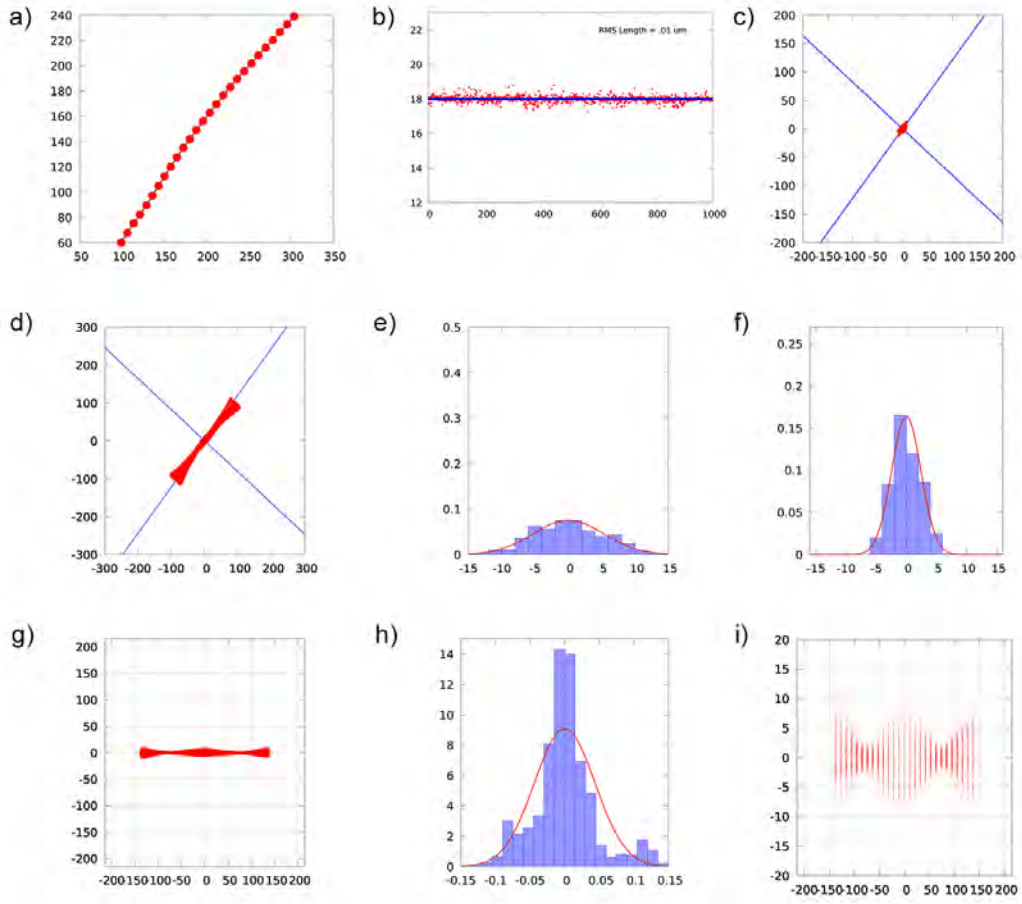

Figure 3.1 a) A typical configuration of the microtubule segmented into 27 segments. b)The length of the tracked microtubule was found by summing the length of each block. The length was measured for each frame. c) The orbit of the center of mass. The ellipsoidal shape is due to the tubular shape of the microtubule. d) Overlap of all MTs configurations available from a recording using center of mass as origin and before the proper rotations. e) The histogram for the orbit of the center of mass along the axis of the distribution in the direction of the microtubule. f) The histogram for the orbit of the center of mass along the axis of the distribution perpendicular to the microtubule. g) Overlap of all MTs configurations available from a recording after the proper rotations. h) Histogram of the rotation angles φ_i, $i = 1, \ldots, N_T$. i) Overlap of all of the beads' orbits from a full recording, after the macroscopic degrees of freedom have been decoupled. The average locations of the beads, to be used as references. Note that the deviation from a straight line configuration is accentuated by the different scales used for the axes.

As shown in Figure 3.1(b) the length displays fluctuations during the recording, which is due to slight movement in and out of focus, but the size of the fluctuations is very small (RMS=1.43%).

3.3.2 Center of Mass

The position of the center of mass for the microtubule configuration in each frame of the video recording can be computed from:

$$\boldsymbol{R}_c(t) = \tfrac{1}{N_B} \sum_{j=1}^{N_B} \boldsymbol{r}_j(t). \tag{3.3}$$

This is a macroscopic variable, which, for a true macroscopic system, will be fixed. In the case of the microtubule, $\boldsymbol{R}_c$ displays fluctuations from one frame to another, akin to the Brownian motion. The orbit of the center of mass of one MT is shown in Figure 3.1 (c). The orbit is referenced from the average position of the center mass, as computed from all the available frames.

There is an anisotropy of the center of mass orbit and the distribution is ellipsoidal in shape. This suggests that the actual distribution is normal, i.e. the probability to find $\boldsymbol{R}_c$ inside the square $[X_c, X_c + \mathrm{d}X_c] \times [Y_c, Y_c + \mathrm{d}Y_c]$ is of the form:

$$\mathbb{P}(\mathrm{d}X_c \times \mathrm{d}Y_c) = \tfrac{1}{\sqrt{\mathrm{Det}(2\pi\hat{\Sigma})}} e^{-\frac{1}{2}\boldsymbol{R}_c \cdot (\hat{\Sigma}^{-1}\boldsymbol{R}_c)}\, \mathrm{d}X_c\, \mathrm{d}Y_c, \tag{3.4}$$

where $\hat{\Sigma}$ is a 2×2 matrix acting on the X and Y components of $\boldsymbol{R}_c$. The entries of $\hat{\Sigma}$ can be found from the correlations:

$$\Sigma_{XX} = \tfrac{1}{N_T} \sum_{t=1}^{N_T} X_c(t)^2,\ \Sigma_{XY} = \Sigma_{YX} = \tfrac{1}{N_T} \sum_{t=1}^{N_T} X_c(t) Y_c(t),\ \Sigma_{YY} = \tfrac{1}{N_T} \sum_{t=1}^{N_T} Y_c(t)^2. \tag{3.5}$$

By diagonalizing $\hat{\Sigma}$ we can find the normal axes of the distributions provided by the (normalized) eigenvectors $\boldsymbol{e}_\alpha$:

$$\hat{\Sigma}\, \boldsymbol{e}_\alpha = \lambda_\alpha \boldsymbol{e}_\alpha, \quad \alpha = 1, 2. \tag{3.6}$$

The directions defined by $\boldsymbol{e}_\alpha$'s are shown as the two axes (1) and (2) in Figure 3.1 (c). The distribution of points is symmetric relative to these axes. The strong anisotropy can only be attributed to the long tubular structure of microtubules. It is expected for the MTs to be strongly displaced by the collisions with the water molecules in the direction perpendicular to their length and only weakly in the other direction. To verify this statement, we overlap in Figure 3.1 (d) all the microtubule configurations available from a recording and the normal axes (1) and (2) and, sure enough, axis (1) is perpendicular to the average longitudinal direction of the tubes.

Furthermore, if instead of X_c and Y_c we use the coordinates defined by these new axes, that is:

$$(X_c, Y_c) \to (X_1, X_2) = (\boldsymbol{e}_1 \cdot \boldsymbol{R}_c,\ \boldsymbol{e}_2 \cdot \boldsymbol{R}_c), \tag{3.7}$$

the form of the distribution becomes:

$$\mathbb{P}(\mathrm{d}X_1 \times \mathrm{d}X_2) = \frac{1}{\sqrt{4\pi^2\lambda_1\lambda_2}} e^{-\frac{X_1^2}{2\lambda_1} - \frac{X_2^2}{2\lambda_2}}\, \mathrm{d}X_1\, \mathrm{d}X_2, \tag{3.8}$$

hence the product of two ordinary Gaussian distributions:

$$\mathbb{P}_\alpha(\mathrm{d}X_\alpha) = \frac{1}{\sqrt{2\pi\lambda_\alpha}} e^{-\frac{X_\alpha^2}{2\lambda_\alpha}}, \quad \alpha = 1, 2. \tag{3.9}$$

As one can see, $\sigma_\alpha = \sqrt{\lambda_\alpha}$, $\alpha = 1, 2$, play the role of the standard deviations. We now can verify the assumption (3.4) by generating the histograms along the axis (1) and (2) from Figure 3.1 (d). They are shown in Figure 3.1(e) and (f) with the Gaussian distributions. The good agreement to a Gaussian distribution gives us confidence that assumption (3.4) is solid.

3.3.3 Macroscopic Orientation

We decouple the center of mass degree of freedom by referencing the beads' positions from the center of mass, in each frame of the recorded videos. Hence, from now on,

we make the change of coordinate:

$$\boldsymbol{r}_j(t) \to \boldsymbol{r}_j(t) - \boldsymbol{R}_c(t), \quad j = 1, \ldots, N_B, \tag{3.10}$$

for each movie frame. To keep the notation as simple as possible, we will continue to use $\boldsymbol{r}_j(t)$ for this new coordinates, hence from now on it is understood that (3.3) gives $\boldsymbol{R}_c(t) = 0$.

In Figure 3.1(d) we overlap again all the configurations of the bead-chains available from a recording, with their mass centers pinned at the origin of the coordinate frame. Our first task is to eliminate the arbitrariness in the orientation of the field of view. While we can definitely define an average orientation, such procedure is not sufficient if our (primary) goal is to study the phonon degrees of freedom. Indeed, by examining Figure 3.1(d) more carefully, one can see substantial fluctuations in the MT's orientation relative to the average orientation. This tells us that there is a meaningful instantaneous angular degree of freedom whose dynamics is interesting to study. The difficulty is that there is no canonical way to proceed.

We decided to proceed by aligning the horizontal axis of the coordinate frame with the instantaneous long axis of inertia of the microtubule configuration. Let us introduce this axis as the line in the plane that minimize the functional:

$$\mathcal{F} = \sum_{j=1}^{N_B} \mathrm{dist}(\boldsymbol{r}_j, \mathrm{axis})^2. \tag{3.11}$$

Note that all factors inside the sum are squared. If we denote the orientation of the yet unknown axis by the normalized vector $\hat{\boldsymbol{e}}$, then:

$$\mathrm{dist}(\boldsymbol{r}_j, \mathrm{axis}) = \left|\hat{\boldsymbol{e}} \times \boldsymbol{r}_j\right|, \tag{3.12}$$

hence:

$$\mathcal{F} = \sum_{j=1}^{N_B} |\hat{\boldsymbol{e}} \times \boldsymbol{r}_j|^2 = \sum_{j=1}^{N_B} (e_x y_j - e_y x_j)^2, \tag{3.13}$$

which can be conveniently written as:

$$\mathcal{F} = (e_y, -e_x) \begin{pmatrix} \sum_{j=1}^{N_B} x_j^2 & \sum_{j=1}^{N_B} x_j y_j \\ \sum_{j=1}^{N_B} x_j y_j & \sum_{j=1}^{N_B} y_j^2 \end{pmatrix} \begin{pmatrix} e_y \\ -e_x \end{pmatrix}. \tag{3.14}$$

Inside the square matrix one can recognize the tensor $\hat{I}$ of rotational inertia. Furthermore, (3.14) tells us that F is minimized precisely when $\hat{\boldsymbol{e}}$ is the eigenvector of $\hat{I}$ corresponding to the highest eigenvalue.

We have implemented the above computations for each frame of the recording and we aligned one axis of the coordinate frame along $\hat{\boldsymbol{e}}$. Figure 3.1(g)shows the outcome of these operations. The procedure eliminates the arbitrariness of the frame orientations. In Figure 3.1(h) we report the statistics of the angles by which each frame has been rotated:

$$\phi_i = \tan^{-1}(e_y/e_z), \quad i = 1, \ldots, N_F. \tag{3.15}$$

They were referenced from the average value of these angles. The histogram is very well characterized by a normal distribution, hence we expect that no systematic bias has been introduced by our procedure of mircotubule alignment.

3.4 Analysis of the Microscopic Vibrational Degrees of Freedom

3.4.1 Vibrational Analysis

In Figure 3.1(i) we overlap the orbits of the blocks during a full recording, after the macroscopic degrees of freedom have been decoupled. We can see the blocks moving around averaged positions $\bar{\boldsymbol{r}}_j$. In the following we will reference the positions from these averaged positions:

$$\boldsymbol{r}_j \to \boldsymbol{r}_j - \bar{\boldsymbol{r}}_j, \quad j = 1, \ldots, N_B. \tag{3.16}$$

To simplify the notation, we will continue to use $\boldsymbol{r}_j$'s, with the understanding that, from now on, $\frac{1}{N_T}\sum_{t=1}^{N_T}\boldsymbol{r}_j(t) = 0$. In Figure 3.1(i), we overlap the coordinates $y_j(t)$ for all the beads and available frames of the recording after operation (3.16) has been implemented.

3.4.2 Nearest Neighbor Correlations

We continue the analysis of the vibrational degrees of freedom by mapping the correlations between pairs of nearest neighbors. The results are reported in Figure 3.2.

The x-y position of each block after decoupling the Brownian motion and the rotation is plotted against the x-y position of its first nearest neighbor, then second nearest neighbor, then third nearest neighbors, etc., for all frames. The distance between first nearest neighbors for the microtubule shown is on average 8 pixels, or .5 μm, and the first nearest neighbors show a high positive correlation. Meaning that as one block moves, the next nearest block also moves in the same direction. After five nearest neighbors, approximately 2.5 μm the circular shape of the scatter plot indicates that the blocks are no longer correlated in their movements. However, after ten blocks of separation, the movements are again correlated, but now they are negatively correlated, or anti-correlated. This means that as the one block moves in one direction, the tenth nearest neighbor is moving with the same displacement on average in the opposite direction.

The transition as you move along the microtubule from correlated movements to uncorrelated movements and then to anti-correlated movements follows from the movement of a wave as it travels along the microtubule. The majority of the movements we are able to capture are first and second mode movements, as is also corroborated in the displacements shown in Figure 3.2(i). For different length

microtubules, the correlation plots will show a different number of nearest neighbors before the movements decorrelate.

Finally, the distribution of the displacements along the principal axes (1) and (2) can be plotted as a histogram for each plot. This is shown in Figure 3.2(b), and each histogram fits a Gaussian distribution. The probability of the measurable displacements, Equation 3.17, being able to be characterized by a normal distribution, Equation 3.18, means that the displacements are due to harmonic interactions between blocks where K represents the stiffness matrix of the system.

$$P_X(\Delta) = \rho(u_1, \ldots, u_N)du_1, \ldots, du_N\Delta(u) = \Delta \cap [-u, u] \tag{3.17}$$

$$\rho(u)(u_1, \ldots, u_N) = \exp(-\frac{\vec{U}\hat{K^{-}}1\vec{U}}{kT}) \tag{3.18}$$

3.5 Discussion

In conclusion, the microtubule was segmented into blocks without a prior assumption of the type of interaction between blocks, and the block configurations were mapped onto a correlation plot after decoupling the macroscopic degrees of freedom. The correlation plot showed how nearest neighbors moved in relation to one another due to thermal excitation. A fit of the distribution of the correlation plots shows that the distribution is Gaussian. A Gaussian distribution is an indicator that the microscopic vibrational properties of the system follows the potential energy distribution of a harmonic oscillator.

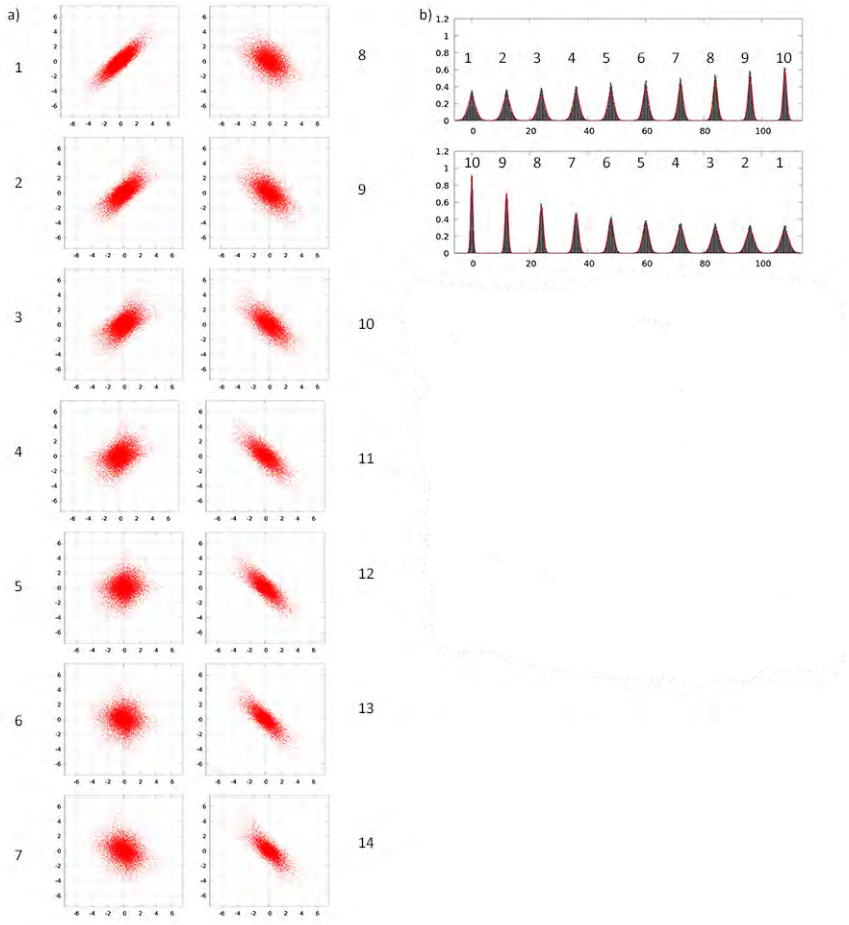

Figure 3.2 a) Correlation plots of x and y positions of the blocks plotted in pairs of first nearest neighbor, then second nearest neighbor, then third nearest neighbors, etc. b) The histograms with their Gaussian fit of the first ten correlation plots along axis(1), top, adn axis(2), bottom.

CHAPTER 4

DIRECT INSIGHT INTO MICROTUBULE HARMONICS: EXPERIMENTALLY MEASURED PHONON SPECTRUM OF MICROTUBULES

4.1 Introduction

In this chapter, a method to measure the phonon spectrum is presented. The method is non-invasive and the data can be collected while the microtubules are *in vitro*, which mimics their natural environment. The focus of the method is to shift from the static to the dynamic characteristics of these unique, self-assembled structures. This method provides a direct insight into the frequency range of bending resonant modes, or transversal modes, of the microtubule, and provides a target frequency range for future experiments that analyze the vibrational properties of the microtubules.

Generic mechanical systems are made of rigid blocks interacting via force fields. In microtubules, these blocks are the tubulin dimers themselves. The force fields are the interaction between the proteins that keeps the microtubule together. Thus, we model the microtubule as a discrete system of N blocks interacting with harmonic potentials. This system has a large number of degrees of freedom leading to a large number of natural collective modes. The actuation of the system is done through a force generated by the thermal energy of the water. This is a time-varying force that is not tuned at all and excites all the collective modes at once with different weights.

The interactions between the blocks of the microtubule are represented by the harmonic potential, V, where K is the stiffness matrix. The thermal energy is derived from the equipartition theorem, $\frac{1}{2}k_bT$, where k_b is boltzmann constant and T is temperature. The thermal energy and the microtubule are in equilibrium, therefore:

$$V_{thermal} = V_{blocks} = \frac{1}{2}k_bT = \frac{1}{2}\sum_{q=1}^{N} Ku_t(n)^2 \tag{4.1}$$

4.2 Derivation of New Math Model for the Mechanical Properties of the Microtubule

In order to glean the material properties from this equilibrium assumption, first, the displacement of each coordinate was calculated in reference to an average position to get N positions for each frame, where N is equal to the number of coordinates:

$$u_t(n), n = 1, \ldots, N \quad t \in [0, T] \, . \tag{4.2}$$

At a fixed time, t, the shape of the microtubule can be modeled by a fourier approximation of these displacements :

$$u_t(n) = u_t(q_0) + \sum_{n=1}^{N} e^{i2\pi qn/N} u_t(q) \tag{4.3}$$

A Fourier transform is used to solve for the unknown fourier coefficients and to go from n to q (mode number). For any fixed time, t, we can encode the information in:

$$\tilde{u}_t(q) = \frac{1}{\sqrt{N}} \sum_{n=1}^{N} e^{i2\pi qn/N} u_t(n) \quad q = 1, \ldots, N \tag{4.4}$$

Using $\tilde{u}_q$'s we can write the energy in a completely equivalent way:

$$U = \frac{1}{2} \sum_{q=1}^{N} F(q)(\tilde{u}(q) - \tilde{u}_0(q))^2 \tag{4.5}$$

Where:

$$F(q) = \sum_{n=1}^{N} e^{i2\pi qn/N} K_n \tag{4.6}$$

The function $F(q)$ can be found from the variance of the Fourier coefficients, which contains information about the stiffness matrix, and therefore, with this, the resonant frequencies of the microtubule can be estimated.

$$\langle(\tilde{u}_q(t+\Delta t) - \tilde{u}_q(t))^2\rangle_{t,\Delta t>\tau} = 2k_BT/F(q) \tag{4.7}$$

Thus the angular frequency can be extracted using the formula below:

$$\omega_q = \sqrt{F(q)/M} \tag{4.8}$$

Where M is the mass of individual tubulin dimers. Finally, the phonon spectrum is plotted as a function of frequency, $f = \frac{\omega_q}{2\pi}$, versus the wave vector, $k = \frac{q\pi}{N}$.

In the long wave limit $\lim_{k\to 0}$ the slope of the linear region of the phonon spectrum represents speed of sound and is an indicator of the stiffness of the microtubule.

$$v = \lim_{k\to 0} \frac{\delta\omega}{\delta k} \tag{4.9}$$

Ideally N would be equal to the number of dimers in a microtubule, but this is not possible due to the resolution of the microscope. A coarse discretization of N=26 using the methods described in Chapter 2, where one block represents 48 rings of tubulin dimers, we obtain 26 modes spread across the whole phonon spectrum. By defining the discretization and increasing N, such that N=50 and 100, the results will represent the reality more accurately. When N increases, the spacing between the natural frequencies decrease and more modes will fill in the phonon spectrum.

4.3 Bootstrapping Method for Persistence Length and Flexural Rigidity Measurement

Next, to ensure that we measure single microtubules, we use a set of standard techniques to determine the flexural rigidity and persistence length and compare it to the ones in the literature. Here it is assumed that the microtubule behaves as a rigid rod.

Table 4.1 Note: This is a table of the persistence lengths and flexural rigidity of microtubules.

Persistence Length and Flexural Rigidity of Microtubules				
	Frames per Second	Length(μm)	Persistence Length(mm)	Flexural Rigidity (10^23 N m^2)
MT 1	10 FPS	8.9	$1.8 \pm .5$	$.06 \pm .02$
MT 2	10 FPS	18.1	$1.0 \pm .1$	$.04 \pm .01$
MT 3	100 FPS	8.25	$.3 \pm .1$	$.01 \pm .002$
MT 4	100 FPS	17.8	$1.1 \pm .2$	$.04 \pm .01$

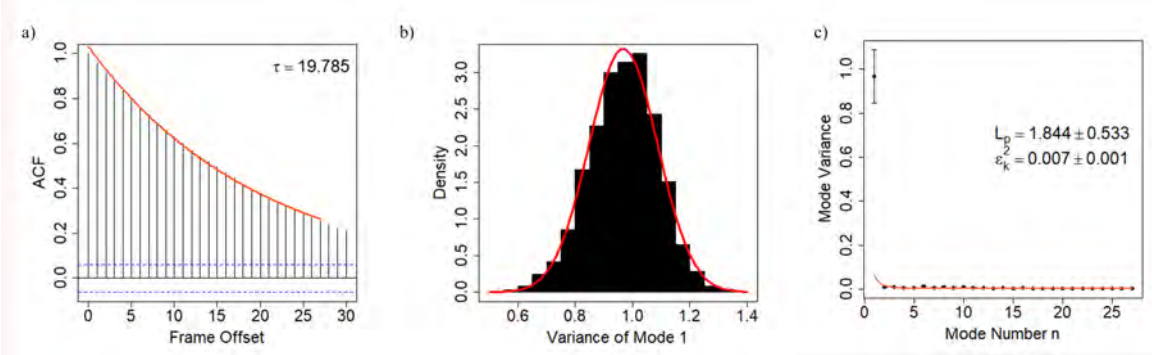

Figure 4.1 (a) Autocorrelation of the variances of the first mode where τ is the decay constant of the exponential fit. The independent number of frames is equal to $N_{ind} = \frac{N_{total}}{\tau}$. (b) A histogram of the variances of the first mode show a normal distribution, illustrating that the bootstrapping method removes the bias introduced by oversampling. (c) The variance for each mode is plotted, and fit to a multiple linear regression model using Equation (2.6).

The persistence length of four microtubules was measured using the bootstrapping method as described in the methods section. The persistence lengths were comparable to those found in the literature for free end microtubules. [35] The data indicates that we measured individual microtubules and that the tracking method is accurate.

For exemplification we present in Figure 4.1 the data for a single 8.9 μm long microtubule. Figure 4.1(a) shows the autocorrelation on the variance of the first mode coefficient in the Fourier series up to 30 frames. The autocorrelation was fit to an exponential that gave a characteristic time constant used to determine the number of independent frames in a single data set of 1000 frames. The distribution in Figure 4.1(b) of the variance of the first mode coefficient is Gaussian, indicating that the bootstrapping method removes bias in the variance measurement due to oversampling. Figure 4.1(c). shows the multiple linear regression fitting of Equation (2.6) to the variance. The multiple linear regression model accounts for the large standard deviation of the first few modes. The first mode shows the largest standard deviation, which is expected as the first mode movement will always have the largest amplitude.

4.4 Experimental Phonon Spectrum of a Microtubule

The phonon spectrum presented here is for the 8.9 μm long microtubule with a persistence length of 1.8 mm. The phonon spectrum was measured using the method described above. Figure 4.2(a). shows the phonon spectrum for the same microtubule segmented into 26, 50, and 100 blocks. The phonon spectrum is plotted as frequency versus k = $\frac{q\pi}{N}$ where N is the total number of segments along the microtubule. The plots show that increasing the segmentation fills in more resonant states for the phonon spectrum. This is because the number of resonant states will be equal to the number of resonators in the system. Figure 4.2(b) shows the fitting of the spectrum in the long wave limit, from which the speed of sound is extracted.

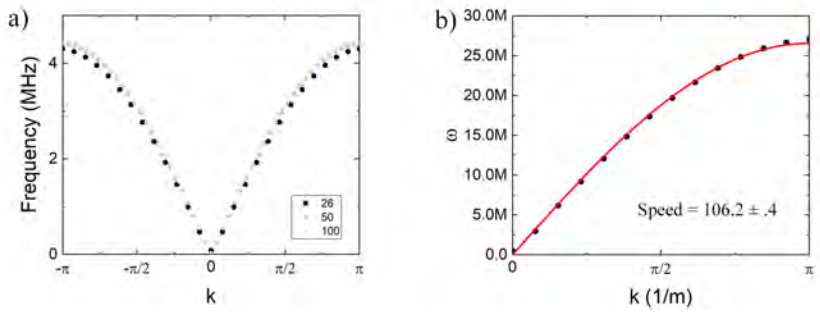

Figure 4.2 (a) The frequencies of the microtubule are plotted against the wave vector, $k = \frac{q\pi}{N}$, where N is the total number of blocks. This is the phonon spectrum of a microtubule segmented into 26, 50, and 100 blocks. (b) The slope of the dispersion, in the long wave limit, represents the speed of sound.

4.5 Discussion

The dynamicity of the microtubule has been observed and studied for decades, but the mystery of how local properties result in the final function of the microtubule is still a topic of intense research.

It is known that the persistence lengths of our microtubules are within the 0.1 - 5.1 mm range showing that the microtubule is a very rigid structure with a persistence length that is an order of magnitude higher than then its actual length.[35] Persistence length and Young's modulus give a quantifiable measurement of the rigidity of the microtubule and these are key measurements in understanding the bulk properties of the microtubule. However, they are not enough for extracting the underlying local interactions of the tubulin proteins. These local interactions, whether they are between taxol-bound tubulins, GTP-bound tubulins, GDP-bound tubulins, or a mixture of all three, are the reason for not only the static, but also the dynamic mechanical properties of the microtubule.

The methodology presented takes the study of microtubules from a continuous model that assumes homogeneity to a meso-scale model of coupled oscillators. This approach expands the methodology to lead to future improvements. It has been predicted theoretically that the MT has a phonon spectrum in the frequency regime of

kHz to GHz. Most calculations fall in the GHz regime for longitudinal vibration modes and Atanasov predicted transverse waves to be in the kHz regime. [42, 43, 44, 41, 45] The loss factor due to damping in the buffer solution has been estimated to be 0.01 up to 1000.[41] Our experimental measurements show that the phonon spectrum of the bending modes of the microtubule lies in the lower predicted frequency regime.

The frequencies measured in the phonon spectrum and the speed at which we are able to image the microtubule affects the experimentally measured velocity. In a discrete model of the microtubule that allows for anisotropy, Shirmovsky et al. predicted the velocity of the wave along the helix direction to be in the range of 147 - 167 m/s, and longitudinal waves velocities 1200 - 1300 m/s.[42] The longitudinal wave velocities are higher due to the stronger bonding along a protofilament. The experimentally measured velocity here is the transverse waves and is smaller than the predicted velocities by other groups. The results presented here are 40 - 140 mm/s.

The microtubule has a fabulous structure. During its self assembly, every time a new dimer is attached to the lattice, there is a release of energy equal to 12 k_bT through GTP hydrolyses. A part of this energy is stored in the lattice as mechanical strain. Thus the microtubule behave as a pre-stressed beam rather than a regular beam. A prestressed beam is more resistant to bending because when bent, the strained is released. When a regular beam is bent, it creates strain, which could lead to cracking. The phonon spectrum obtained here does not resemble the a phonon spectrum of a regular beam for which the restoring force is proportional to the square of the displacement. It resembles more a phonon spectrum of a pre-stressed beam for which the force is linear with its displacement.

The method proposed here is limited because it assumes uniform and harmonic interaction between blocks. It also only measures transversal modes, rather than all existing modes. Finally, it uses the thermal energy of water to excite the modes, rather than providing a controlled excitation.

Future experiments must be done to excite and measure other modes of the microtubule. One has to go beyond thermal energy and engineer actuators to excite the longitudinal and torsional modes for a complete picture local properties of the microtubule as well as to study the local differences between bovine brain and cancer derived microtubules, or the effects and efficiency of different pharmaceutical compounds, such as chemotherapy drugs.

CHAPTER 5

MEASUREMENT OF CHANGES IN LOCAL STRUCTURAL PROPERTIES USING A CORRELATION MATRIX

5.1 Introduction

The reason dynamic instability is not well understood is because the link between the microtubule structure and its dynamics are not well measured. The structure of the microtubule must be thought of differently and the approach to measure it must be reevaluated. Therefore let's approach the microtubule not as something that evolutionarily developed to be mechanically sound, but rather to be dynamically sound as a collective system.

It has been shown that microtubules of different isotypes have a direct impact on the shortening rates of the microtubule, which points to the fact that local properties affect system dynamics, but the measurement techniques currently used do not give a way to measure these changes in local properties. [46] Without a way to better understand the anisotropic structure of the microtubule, it will be impossible to measure experimentally or even simulate the true dynamics of the microtubule and to be able to predict how its dynamics can be affected in regards to cancer therapy and chemotherapy drug resistance.

If we are able to measure and map the microtubule movement at different points along the microtubule, we will be able to prove that there are quantifiable differences in the local structural properties of a microtubule made of different tubulin isotypes. We will then be one step closer to measuring the true dynamic modes of the microtubule.

The method presented here is effective in doing just that. Utilizing methods developed for disordered colloidal systems, we measure changes in the local inter-

actions between breast cancer, cell line MCF-7, derived tubulin and bovine brain derived tubulin within a single microtubule.

5.2 Cancer Derived Microtubules Show Differences in Local Mechanical Properties from Standard Bovine Brain Derived Microtubules

Ghosh et al. developed a method to use concepts from solid state physics to measure the density of vibrational states of a colloidal system. They did so by constructing a displacement correlation matrix of a two-dimensional colloidal system and solving for the eigenstates.[47] Islam et al. took this method a step further by introducing disorder in the interactions between colloid particles.[38] He measured the probability distribution of the temporal fluctuations to get the degree of disorder in the system. He also used the displacement correlation matrix to measure the density of states of the disordered colloidal system.

We applied a similar technique to change the approach to studying the vibrational properties of the microtubule. We constructed a correlation matrix of the changes in angle between segments along the microtubule over time. The matrix plot is a measure of the degree of correlation between first nearest neighbors, second nearest neighbors, third nearest neighbors, and so forth.

The more segments that are correlated means that the movement is correlated for longer distances. The stiffness of the material is indicated by the distance along the material that the bending angle is still correlated. The homogeneity in stiffness is shown by the uniformity of the correlation pattern from segment to segment. The MCF-7 derived segments break this uniformity and this can be measured using the correlation matrix plot. Changes in the correlation measurement are an indicator of local changes in stiffness. The differences in stiffness between segments of a microtubule made of cancer derived tubulin and bovine derived brain tubulin are shown in Figure 5.1. This is a result of the different distributions of tubulin isotypes

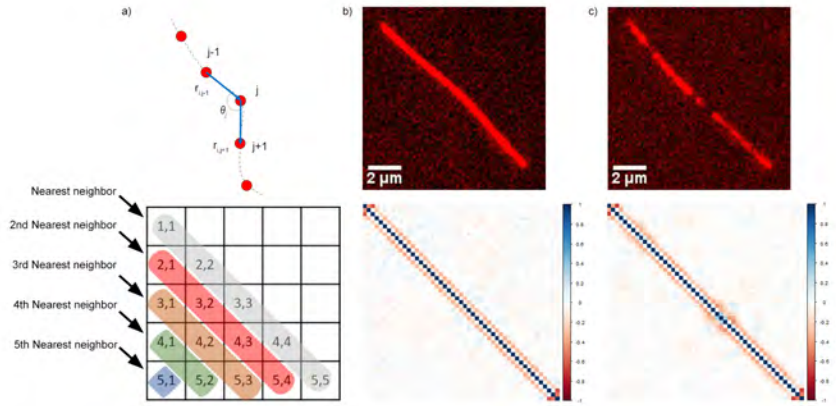

Figure 5.1 a) A chain of segments is shown as a representation of the angles that were measured along the microtubule. The angle is between two segments along the microtubule. The correlations of the first nearest neighbors, second nearest neighbors, etc. are shown where they are mapped onto the correlation matrix plot. b) A microtubule made from MCF-7 derived tubulin was uniformly mixed with 10%Alexa-594 labeled bovine brain tubulin and its angle correlation matrix. c) A segmented microtubule made from MCF-7 derived tubulin and bovine brain tubulin. The dark regions are the MCF-7 tubulin segments. The correlation matrix shows a change in the angle correlations at the locations where the MCF-7 derived tubulin segments are and show more flexibility.

that make up MCF-7 derived tubulin and bovine brain tubulin. MCF-7 derived tubulin is 55% β-I, 6% β-III, 39% β-IV, and bovine brain tubulin is 3% β-I, 58% β-II, 25% β-III and 13% β-IV.[29, 31] Figure 5.1 shows that there is a change in the stiffness of the MT at these localized regions of MCF-7 tubulin which are highly concentrated in β-I and β-IV tubulin proteins.

In the regions where there are a majority of tubulin from the cancer derived microtubtules we see anti-correlation between segments, which means the microtubule is more flexible in these regions.

5.3 Using Bending Angles to Measure Changes Allows for a Measure of Independent Modes

Figure 5.2 shows the correlation of the angle between segments along the microtubule plotted as a scatter plot. It can be seen that the angles decorrelate by the second nearest neighbor. This is important because in order to measure the true dynamic

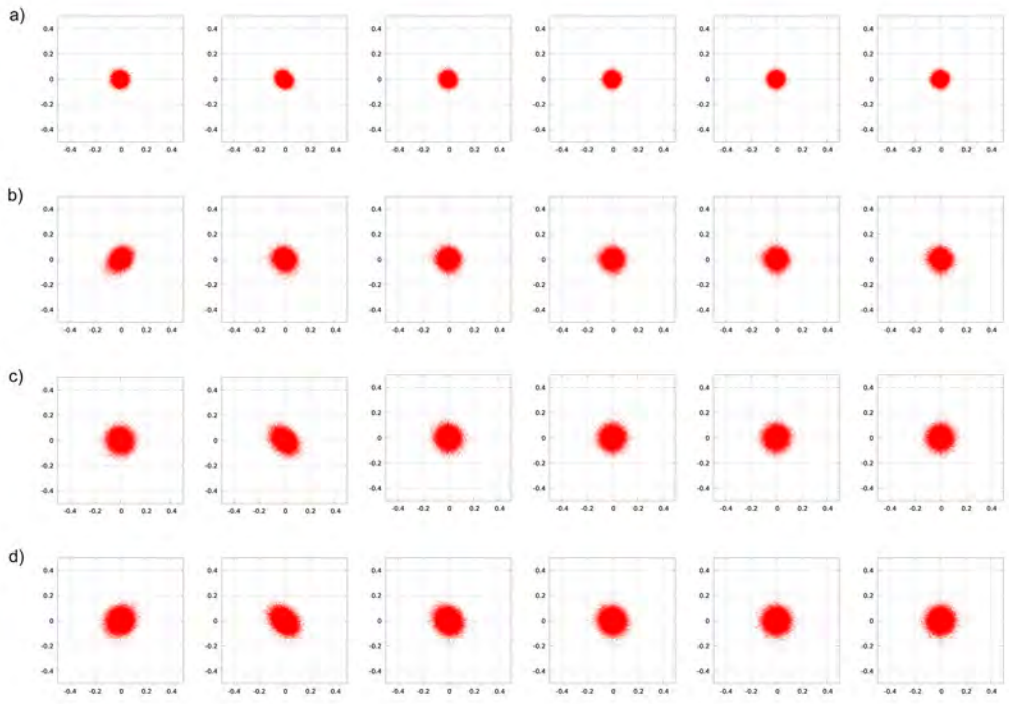

Figure 5.2 a) Bovine brain microtubule b) Microtubule made of MCF-7 derived tubulin uniformly mixed with 10%Alexa-594 labeled bovine brain tubulin. c) Microtubule made of Hela derived tubulin uniformly mixed with 10%Alexa-594 labeled bovine brain tubulin. d) Segmented microtubule made from MCF-7 derived tubulin and bovine brain tubulin. The x-y position of each segment is plotted against the x-y position of its first nearest neighbor, then second nearest neighbor, then third nearest neighbors, etc.

resonant modes of the system without bias, the measurements must be a random distribution of its motion. This result is indicative of our correlation plot to be due to a random sampling of the configuration space of the microtubule. Therefore, there is no bias introduced due to lower resonant modes having larger amplitude movement, as is seen with standard persistence length measurements.[35] The difficulty is, however,

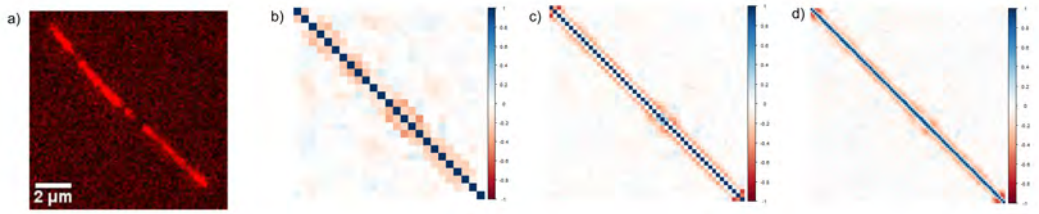

Figure 5.3 Correlation plot of a segmented MT made of MCF-7 derived MTs and bovine brain MTs segmented into 26, 50, and 100 segments.

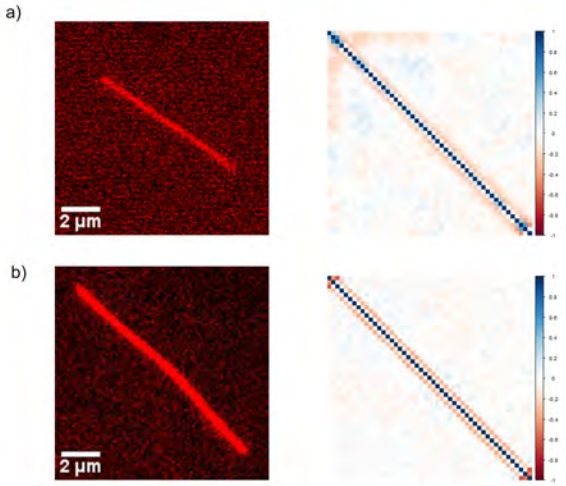

Figure 5.4 a)Bovine brain MT and correlation plot with 50 segments. b) MCF-7 derived MT and correlation plot with 50 segments.

that we would need at least 20,000 data points in order to have enough sampled data to measure the dynamics of the system with statistical significance.

5.4 Resolution of Detecting Changes in Properties is Dependent on the Segment Length

Increasing the number of segments allows for more precision in measuring local changes, but the drawback is that angles between smaller segments are susceptible to more error in tracking due to noise in the image.

Furthermore, if we wanted to see local changes at the protein level, this would be difficult with this current method. Figure 5.4 shows that there are no discernible

differences seen along the stiffness properties of the MTs because the distribution of tubulin isotypes is more uniformly distributed, and so to be able to see local changes in these MTs we would need protein level tracking accuracy.

5.5 Discussion

Using the methods presented here we have applied standard methods in colloidal studies to a biological material. The correlation plots of microtubules shows that microtubules made up of different distributions of tubulin isotypes have different local stiffness.

The difference in local mechanics presented here is most likely due to tubulin isotypes having small differences in their structure, which impacts the longitudinal and lateral interactions along the microtubule. [48, 49] What we have shown here is that a higher density of β-I and β-IV isotypes is more flexible than a higher density of β-II and β-III isotypes. This concurs with what Derry et al. showed in their study of the growing and shortening rates of microtubules made of varying tubulin isotypes compositions.[11] The growing rates were on average the same for all microtubules of different isotype compositions because the growing rate is determined largely by the diffusion rate of free tubulin to the growing end of the microtubule. However, the shortening rates varied significantly between microtubules of different isotype compositions. This makes sense if we look at the shortening rates as being reliant on the amount of energy available to the microtubule. The more energy there is available, the more energy can be used to pull apart the lateral bonds holding the protofilaments together and thus the shortening rate will be faster. The less energy available, the slower the shortening rate will be. The energy we speak of here is the energy stored in the structure of the microtubule itself or, more precisely, in the bonds between the tubulin proteins. Stronger bonds require more energy to break, and also result in a stiffer material. Weaker bonds require less energy to break, and also result in a more flexible, softer material. Therefore, the results show that β-IV bonds are

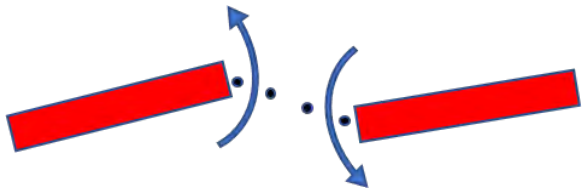

Figure 5.5 Representative segmented microtubule where the blocks represent regions of bovine brain tubulin and the dotted line represents the region of MCF-7 tubulin. The arrows indicate the direction of motion.

more flexible, and therefore the bonds are weaker and there is less energy available. Derry et al. shows that microtubules consisting of only β-IV tubulin have the slowest shortening rates compared to β-II, β-III, and mixed tubulin microtubules.[11]

The regions of bovine brain tubulin on either side of the regions of MCF-7 tubulin show anti-correlation motion meaning the segments are moving in opposing directions. A representation of this concept is shown in Figure 5.5 This suggests a structure where the regions of bovine brain tubulin are linked by more flexible regions of MCF-7 tubulin. In order to improve this method, we need to improve the identification and tracking of the different tubulin isotypes. This could be achieved by labeling different isotypes with different fluorescent dyes, which can be difficult as this is not commercially available and would need to be produced in house. The regions of no fluorescence cannot be accurately tracked with the current method; the only information we can extract on the stiffness of the MCF-7 segments relies on the changes in angle of the segments on either side of the darker regions. For tracked segments that are smaller than the length of the dark segments, this will show an artificial positive correlation between nearest neighbors. Therefore, the number of segments the microtubule is segmented into must be chosen to not be smaller than the longest MCF-7 region.

This method is the first step towards measuring the phonon spectrum to obtain the true dynamic vibrational modes of the microtubule. This step is definitely

challenging with microtubules because of the relatively short life span of microtubules in vitro and because precise tracking can be difficult.

The phonon spectrum measurement of a colloidal system depends on three things. First, it depends on tracking of the displacement over time of each particle with no missing data points, which can occur if the particles move out of focus during the video. The tracking must also ensure the accurate tracking of the same particle over time and not mistaking one particle for another, which can happen if the particles move large distances between frames. Second, data must be sampled with a long enough time lag to extract the independent resonant modes of the system. When the time lag is long, the displacement of each particle is completely decorrelated from one frame to the next. This allows for a dataset of random, uncorrelated, and therefore independent snapshots of the system. This dataset of independent displacements can then be solved for its eigenvalues to get the resonant modes of the system. Third, the dataset must be large enough to be statistically significant. Islam et al. showed they needed 20,000 independent data points to get a histogram of the vibrational energy states, or the density of states. To get a data set this large took days of continuous imaging of the colloid system. This approach is not feasible for measuring microtubules because the bleaching of the fluorescent dyes on microtubules only allows for a few minutes of imaging.

The problem of bleaching could be resolved by using quantum dots, which do not bleach, attached to the microtubule. Another method could be to use the sampling method called bootstrapping to extract independent frames from a smaller dataset. The bootstrapping method uses an autocorrelation function to determine a characteristic time, τ_c, at which the frames decorrelate from one another, and then divides the total number of frames by τ_c to get the number of independent frames, N_{ind}. The dataset can then randomly sampled to select N_{ind} frames, solve the for the resonant frequencies modes, and then repeat this 5000 times for new randomly

selected N_{ind} frames. This would produce a phonon spectrum of the resonant modes with a measure of the error associated with each resonant mode. If we wanted to get away from imaging all together, yet another solution could be to use electrodes to measure small movements along the microtubule. The tubulin has a net negative surface charge that would cause the microtubule to act as a dieletric between two electrodes, and as the microtubule moves, the movement of the surface charge could create a measurable change in capacitance between the electrodes. [50, 51, 52] In order to achieve this the electrodes would need to be embedded in a nanofluidic platform and be on the scale of nanometers to a few microns to be able to measure at multiple points along the microtubule.

CHAPTER 6

EXPERIMENTAL PLATFORM FOR ISOLATING SINGLE MICROTUBULES FOR IMPROVED STRUCTURAL ANALYSIS

6.1 Introduction

The development of techniques in nanofabrication has become an increasingly useful tool in the life sciences. [53, 54, 55, 56] Methods that are developed for nanofluidic channels are significantly useful in designing and fabricating nanofluidic devices that are adaptable for microscopy and that can integrate electronics for sensing and actuation of single proteins or macromolecules. [57, 58, 59]

Single proteins and macromolecules are typically imaged at high magnification using fluorescence or bright-field microscopy. This requires imaging through a thin optically transparent material, typically glass or fused-silica. Furthermore, the ability to adapt nanofluidic devices for electrodes to incorporate manipulation and sensing requires the nanochannels to be in an insulating material, and this is another benefit to fabricating in glass or fused-silica. However, it is difficult to seal the nanochannels by bonding directly to a glass or fused-silica coverslip with no intermediate layer. [60, 61, 62, 63, 64, 65, 66, 59]

Currently there are a variety of methods to seal micro-nanofluidic channels. A common bonding material is PDMS. PDMS bonds strongly to glass and fused-silica, and is easy to use, cheap, and readily available. However, since PDMS is elastic it can collapse and block channels that do not have a high aspect ratio. [60] This limits the geometries for which you can seal the fluidic channels successfully. Glass and fused-silica are also able to be bonded using direct bonding. Glass or fused-silica surfaces that are highly clean and have low surface roughness will attract each other in a reversible van der Waals bond. After annealing at high temperatures, this bond becomes permanent. [61] This method has shown success in sealing nanofluidic

channels.[62, 63] However, it requires high temperature furnaces in a clean room environment, which is not always easily accessible. The high temperatures may also distort the channels walls, and compromise electrodes embedded in the device.[64] Low temperature direct bonding (less than 200 C) has also been been successful using plasma activated surfaces, but the surface roughness must be well controlled.[65, 66, 59]

In conclusion, we present a highly repeatable and detailed method for interfacing microchannels with 150 nm wide by 300 nm deep nanochannels and capping them with a glass coverslip using sodium silicate as a bonding medium. The bonding is done outside the cleanroom and does not require expensive equipment. The nanochannels are milled into fused silica using focused ion beam that can be used to mill features down to 4 nanometers.[67, 68] This device can be used for transmission and fluorescence microscopy at high magnification with low fluorescence background. This method can be adapted to include electrodes in the nanochannels for sensing and actuation with dimensions that promote high signal to noise ratio.

6.2 Fabrication of FIB Nanofluidic Channels in Fused Silica

6.2.1 Fabrication of Micron-sized Channels

The devices were fabricated on 500 μm thick fused-silica wafers with a diameter of $d = 76.2$ mm. The wafers were cleaned in a Piranha solution 3:1 H_2SO_4:H_2O_2 for 5 minutes, followed by a DI water bath for 1 mintue. The wafers were rinsed with DI water and dried with N_2. Next, the wafers were placed in an isopropyl alcohol (IPA) bath for one minute, followed by a DI water bath for another minute. Afterwards, the wafers were rinsed with DI water and dried with N_2.

Next, the wafers were primed with hexamethyldisilazane (HMDS) in a Yield Engineering Systems (YES) HMDS prime oven at 148 C. The procedure dehydrates

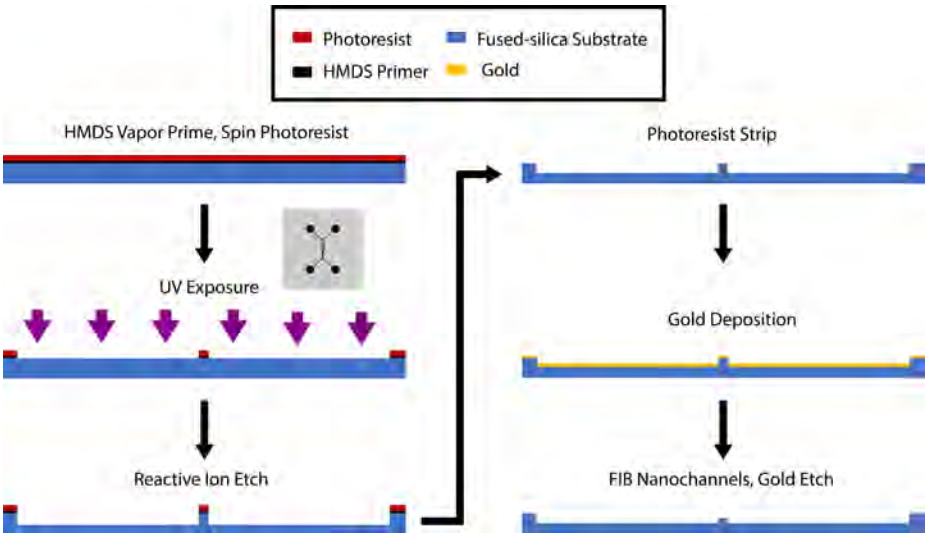

Figure 6.1 Cross-sectional nanochannel process flow. Directions of steps indicated by arrows. First, start with an HMDS vapor primed fused-silica wafer coated in 1.8 μm AZ1518 photoresist. Next, perform UV photolithography exposure with indicated photomask. RIE exposed pattern to etch it into the substrate. Strip wafer in microposit remover 1165 photoresist stripper at 70 C. This allows micron-sized channels of width, $w = 50\mu$m, and depth, $d = 1.5\mu$m to be present on substrate. Prepare wafer with 15 nm gold for FIB milling. Gold etch after milling.

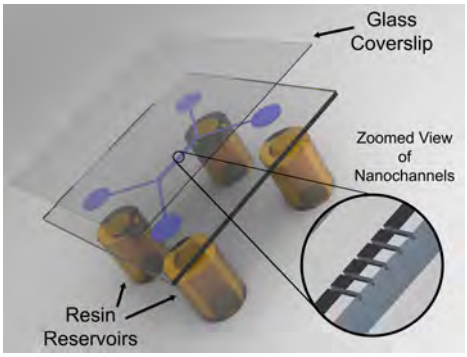

Figure 6.2 Rendered CAD model of the microchannel device integrated with the nanochannels. Nanochannels are highlighted by the zoomed view insert. Imaging is done through the glass coverslip with an inverted microscope.

the wafers and then vapor primes them with HMDS. Next, AZ1518 positive photoresist is spun on the wafers at 4000 RPM for 44 s. The wafers are baked for 2 minutes and then cooled on a cooling plate. Standard photolithography is performed for 30 s using a Karl Suss MA6 mask aligner to expose the sample with

the micron-sized channel pattern shown in Figure 6.2. The wafers are manually developed in AZ300 MIF for 60s.

Wafers are measured with a KLA Tencor P15 profilometer to verify that the photoresist was properly removed from the patterning area. Next, the wafers are placed three at a time in an Oxford PlasmaPro 80 Reactive Ion Etch (RIE) and an O_2 descum is run for 2 minutes to remove any residual resist from the microchannel structure due to exposure and development. Next, an SiO_2 etch is performed for 1 hour and 15 minutes. The etch is a combination of CHF_3 and Ar gasses at 15 sscm and 35 sscm, respectively. The RF reflected power is between 4 and 5 W and the DC bias is between 444 and 450 V. The wafers were measured with the profilometer to verify the etch depth. The photoresist is stripped for 1 hour in Dow Microposit Remover 1165, and the final depth of each channel is measured once more in the profilometer.

In order to prep the fused-silica substrates for focused ion beam (FIB) milling, they are coated in 20 nm of gold in an Angstrom Nexdep E-beam evaporator. The wafers are then coated in AZ1518 photoresist and diced into 22 mm x 22 mm chips. After dicing, the photoresist is stripped in 1165 for 15 minutes to prep devices for FIB milling.

6.2.2 Focused Ion Beam Milled Nanochannels

Nanochannels are milled between the micron-size channels using an FEI Helios G3 DualBeam FIB/SEM or an FEI Helios 600 Dual Beam FIB. Up to two devices were loaded into the FIB chamber at a time. The SEM is used to focus on the sample surface to determine the z-axis working distance and locate the milling area on the sample. Milling the sample with the ion beam requires focusing on the surface and aligning the ion beam's focal point to the electron beam's focal point. To align the two beams, the ion beam is moved to match the field of view seen by the electron beam.

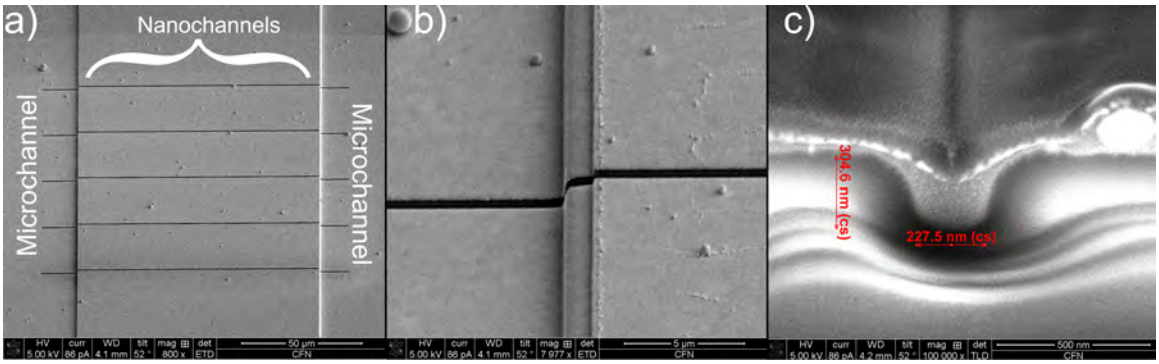

Figure 6.3 a) SEM image of microchannels integrated with five FIB milled nanochannels. b) 7,977x magnification of one nanochannel indicating the junction between the micron-sized and nano-sized channels. c) FIB cross section of a single nanochannel acquired after platinum deposition.

Next, the ion beam is focused at a low current. An ion beam at 30 kV and 18 pA can be used focus the image without destroying the sample surface. Once the image is focused, the procedure must be repeated at the voltage and current that will be used for milling in an area away from the final area to be milled. The depth is defined at 300 nanometers in the milling settings. FIB milling was done at 30 kV and 24 nA for up to five nanochannels as shown in Figure 6.3a. The depth of the nanochannels was characterized by coating the surface of the milled region with a layer of platinum and the ion beam was used to mill a cross section of the nanochannels as shown in Figure 6.3c.

After FIB milling, a gold etch was performed on the samples to remove the Au coating. They were cleaned using an RCA-1 cleaning protocol for 15 minutes, coated with AZ1512 photoresist, and transported to the lab for bonding.

6.2.3 Packaging Fluidic Channels

Port holes were drilled into the ends of the micron-sized channels using a drill press at 3600 rpm using a diamond coated drill bit of 0.5 mm diameter.

To seal the devices, a modified quartz bonding protocol is executed as reported in Wang (1997) and Khandurina (2000).[69, 70] Ideally, the protocol is executed in a

cleanroom, but for the reported devices, it was performed in a laminar flow hood in the lab. To prepare for the sealing of the nanofluidic devices, it is critical that the benchtop, fume hood, and laminar flow hood be as clean and dust-free as possible. They are all cleaned with 70% ethanol and again with IPA. A Ni-Lo 4 XL vacuum holder digital spin coater is cleaned, lined with fresh foil, and set to 4000 RPM for 10s with 500 RPM ramp speed. A DI water bath is heated on a hotplate in the fume hood to 70 C and a smaller beaker of 40% wt. potassium hydroxide (KOH) is suspended within. The KOH beaker is covered with aluminum foil to keep it dust-free. Two large beakers are filled with DI water from a Millipore DirectQ-3 UV for rinsing and placed by the hotplate for transfer of the samples from KOH and in the lamniar flow hood. In order the minimize dust, both beakers are covered with aluminum foil.

A 7% sodium silicate solution is prepared by diluting 70 μL of sodium silicate in 1 mL millipore water. 1 mL of the solution is filtered into an Eppendorf tube. Next, a fresh piece of lens paper is taped down in the laminar flow hood and a Petri dish cover is kept nearby to provide a place to keep the dried devices awaiting bonding. Three sets of tweezers are cleaned with IPA and dried. If bonding is executed in a cleanroom, it is still recommended to clean all surfaces, glassware, and tweezers, but the environment should be sufficiently dust-free for the procedure.

Photoresist is stripped from the diced devices with 1165 microposit remover for 15 minutes at 70 C before the bonding procedure begins. The devices and 22 mm x 22 mm coverslips are cleaned by placing them in a chemically resistant coverslip rack and sonicating them in acetone for 5 minutes. Devices and coverslips are rinsed in the rack sequentially with acetone, IPA, ethanol, and DI water. The loaded coverslip rack is placed in a beaker of DI water which is covered with aluminum foil to minimize exposure to particulates.

One device and coverslip are carefully loaded into the heated KOH for cleaning. If this process is being performed in a cleanroom, substitute the KOH with RCA-1.

After 2 minutes, the device is removed from the solution and place in a beaker of DI water. It is moved to the laminar hood and transferred to a second beaker of DI water. The device is then removed from the beaker and dried thoroughly with N_2. It is placed channel-side up on the lens paper and covered with the Petri dish cover. Repeat these steps for the coverslip, but do not place it on the wipe after drying with N_2. Rather, load it into the spinner and spin dry.

Next, a pipette is used to add 7% sodium silicate solution on the coverslip and it is spun at the settings listed above. Once completed, the sodium silicate coated coverslip is removed with dry tweezers and placed coated side down on top of the device. The coverslip is gently pressed down on with the blunt end of the tweezers and the bond visibly forms between the device and the coverslip. To seal multiple devices, repeat these steps while leaving the sealed devices under pressure of some weight.

The sealed devices are transferred to a clean, foil-covered hotplate at room temperature for annealing and a weight (e.g., a clean, empty beaker) is placed atop the device. The temperature is set to 90 C and left for 24 hours. Afterwards, the hotplate is turned off and is left to cool. Room-temperature annealed devices are stored in deionized water until needed.

Fluorescent liquid was flowed into the final device to test the quality of the seal and ensure that the nanochannels can be filled with liquid via capillary action as shown in Figure 6.4. The fluorescent liquid was made by hydrating fluorescein in DI water to make a 1 mM concentration solution. Fluorescein is sensitive to blue light, so solutions were made in with red or yellow light and foil was used to cover any containers to prevent bleaching of the sample before imaging. The 1 mM fluorescein solution was stored in the refrigerator and showed high fluorescent activity even after six months of storage. The nanochannels were imaged at 100x magnification with a 1.6x optovar to increase magnification. The fluorescein solution flowed into the

nanochannels by placing a drop of solution at one port on the left micron channel, the nanochannels began filling up with liquid within five minutes, and once that was observed we placed another drop at the port of the right micron channel.

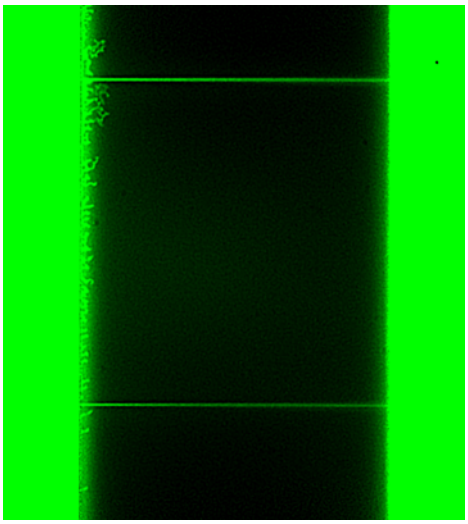

Figure 6.4 Image of nanochannels filled with fluorescein imaged at 100x with fluorescent microscope.

6.3 Discussion

The cleanliness of the wafer is critical for each stage of the process. Any particulates on the surface can block the fluidic channels or cause an uneven photoresist deposition. Wafers that were not cleaned properly at each step did not have precise patterning of the microchannels due to uneven photoresist, and this caused jagged edges on the microchannels. Photoresist also does not adhere well to fused-silica. Priming the wafers with HMDS was a necessary step to promote the adhesion of the photoresist to the wafers.

The profilometer measurements are important to verify proper photoresist development, the etch rate of the RIE, and the final depth of the microchannels. Photoresist AZ1518 is 1.8μm in depth, and the profilometer measurement after the photoresist was developed verified that the photoresist is removed from the

microchannels and the wafer is set for etching. The RIE etch process etches both the fused-silica and the photoresist with different selectivity, so the etch time for a specific depth must be determined. The wafers are etched for different times, and profilimeter measurements are performed for each time to determine the etch rate. An etch time of 1 hour and 15 minutes resulted in a 1.2 μm deep micron channel.

The FIB milling was done on two devices at a time. On FIB/SEM tools that do not have a separate sample loading chamber it can take 15 to 30 minutes to pump down the sample chamber to vacuum. Therefore, using a stage holder that can hold the whole wafer is preferred. However, newer FIB/SEM tools have a sample loader that minimizes the pump down time to only a couple minutes. This provides the flexibility to dice the wafer before the milling step. It is preferred to dice the wafer before milling because dicing is not a clean process and there is more risk of clogging the nano-size features.

The gold coating on the samples is necessary for SEM imaging. Fused-silica is non-conductive, and therefore charging effects due to the SEM makes it difficult to image. Charging occurs when the electrons do not have a conductive path to guide them away from the sample surface and a layer of electrons is generated. The cloud of electrons prevents clear projectile of the secondary electrons from the surface to the electron detector, resulting in poor image quality. The gold coating provides a conductive path the the electrons to move away from surface during imaging. However, long exposure to the electron beam still resulted in charging effects.

The milling step of the process is achieved by shooting a focused beam of Ga+ ions at the surface of the material. The mass and acceleration of the ions allows for milling of the material, and it also acts as another method for imaging by detecting secondary electrons ejected by the sample surface. The secondary focusing of the ion beam is a difficult step because this step is destructive to the surface so it must be performed quickly and in an area away from the final area to be milled. Additionally,

the layer of gold is thin and easily stripped by the ion beam also making it difficult to focus. If the ion beam is not focused well the channels will not be precise in width and will not be deep enough. The difficulty of the focusing of the ion beam causes variability in the depth and width of the nanochannels across devices. The widths of the nanochannels were on average 230 nm, and the heights of the nanochannels were on average 300 nm.

The bonding process is robust, repeatable, and does not result in any clogging of the channels. The bonding requires the coverslip and the device to be pressed together for at 3-5 minutes to allow for good bonding that bonds a majority of the surface. A successful bonding can be seen by eye by a change in contrast between the coverslip and the fused-silica. If the bonding is not successful, then the device can be sonicated in acetone to seperate the two pieces. The bonding procedure can be repeated on the device and a new coverslip, but it is more difficult to have successful bonding the second time. It is also preferred to make the substrate with the channels to be smaller than the coverslip because the sodium silicate is most uniform and flat in the center of coverslip.

The drilling of the port holes can be difficult and result in cracking the device. This can be avoided by securing the device with a shock absorbing material, such as tape or by sandwiching the device between two glass slides. It is also important to use a high precision drill and have control over the speed with which you drill through the fused-silica. The drilling must also be done with the device submerged in water or with a droplet of water at the drilling site. This prevents over-heating of the fused-silica and prevents the glass particles from floating into the air.

In conclusion, flow through a through a 300 nm channel is reported using a method to seal the fluidic channels that allows for easy imaging with a microscope. This methodology allows for an adaptable tool to isolate and measure single proteins and macromolecules to perform direct and quantitative measurements. The reported

device is also adaptable to fabricating electrodes along the channel as an added sensor to detect and measure in the nanochannel. The small dimensions of the nanochannel are crucial for the addition of electrodes: to increase the signal to noise ratio, the electrodes need to be close enough to the object of study to minimize electrical signal from the solution itself.

The use of nanofluidic platforms has already benefited the study of DNA's unique structural properties. The adaptability and repeatability of the fabrication of the devices presented here makes it an ideal platform to open the doors to isolate and study not only DNA, but also other proteins and protein assemblies. For example, the nanochannels can be milled to an ideal height and width to isolate single actin or microtubule proteins. These biopolymers have unique polymerization and depolymerization properties that need to be quantitatively measured at the protein level to elucidate the dynamic mechanics of these structures. This platform allows for variations in size that can be optimized for the object of study. Furthermore, this platform affords the ability to isolate and manipulate macromolecules and proteins for measurements, while keeping their naturally aqueous environment.

CHAPTER 7

CONCLUSION

Theoretical simulations of the microtubule phonon spectrum show that it is highly important to be able to measure the phonon spectrum of a microtubule to understand the mechanics of the microtubule lattice and dynamic instability. Microtubules are predicted to be naturally occuring topological phononic crystals, and the localization of vibrational energy in topological phononic crystals are predicted to be the mechanism for dynamic instability. This insight into the mechanism behind dynamic instability will pave new pathways for chemotherapy drug development and provide inspiration for new self assembling nanoscale materials.

The methods presented here could be further enhanced to provide a window into the local mechanical characteristics of microtubules, such as the protein-protein force fields, at scales fine enough to detect the presence and the effect of various proteins, such as motor proteins, and chemical compounds, such as the chemotherapy drug Taxol. In order to reach these fine scales we cannot use standard microscopy techniques. Instead, an experimental platform must be fabricated that can measure movements of the microtubule at micron or even nanometer precision. This could be achieved with nanometer scale electrodes built into a nanofluidic device. The tubulin protein has a net charge, and if the microtubule moves relative to electrodes placed along its length the movement could be sensed capacitatively. Fabricating such a device is not far from realization with the advent of e-beam lithography, better packing techniques for fluidic platforms, and with new developments in the use of carbon nanotubes as nanoscale electronic sensors.

The other major hurdle in measuring the phonon spectrum of a microtubule, is that a microtubule's natural environment is aqueous and so even if the microtubule

is actuated at high frequencies there is too much damping due to the water. One way to overcome this is to get the phonon spectrum of the microtubule using the dynamic correlation matrix. Damping is a function of momentum, so if we can construct our model to extract the resonant frequencies of the microtubule based on its potential energy function we can decouple the momentum energy and potential energy and have just a measure of the system without damping. To do this we can solve for a Boltzmann distribution of the possible vibrational energy states with the free energy being only a function of $U = \frac{1}{2}Ku^2$, where K is a matrix of stiffness constants and u is displacement. However, the problem is that we do not know K and we need a way to accurately measure K. This is how a dynamic correlation matrix can be utilized. The dynamic correlation matrix has been used in colloidal studies to get the density of states of a 2D system of spherical colloids interacting due to thermal fluctuations at room temperature. Each colloid particle is tracked, and the correlation of the displacements of each particle is mapped onto a 2D matrix. In order to construct the dynamic correlation matrix the displacements measurements over time must be independent from one measurement to the next and there must be a large enough data set to sample all possible configurations of the system. For Islam et. al. this meant a time lag of 1 second between measurements and 20,000 displacement measurements. Therefore, to get a measure of the possible energy states of the microtubule using displacement measurements we need a data set that is taken over a long time to get independent displacement measurements and has at least 20,000 independent displacement measurements. Initial estimates show that to get independent displacement measurements we need to take measurements every 40 seconds.

By applying analysis techniques used in solid state physics we were able to develop a statistical model to measure that the interactions between tubulin dimers are harmonic in nature, and by applying concepts in colloidal soft matter physics we

were able to redefine how to model the vibrational modes of the microtubule and be able to measure localized changes in structural properties. These methods lay the foundational steps needed to measure the true phonon spectrum of the microtubule.

The study of the structure and dynamics of the microtubule can also be the basis for a new class of smart nano-materials. Biological materials, like the microtubule, can serve as inspiration for discovering new materials displaying radically new surface physics. Imagine a material that, based solely on the properties of its building blocks, can self-assemble into a material that can transport mechanical energy without dissipation. Nature has evolutionarily figured out a way to do this, so let's be inspired by what nature has perfected and open our minds to a plethora of novel applications in energy transfer and materials manufacturing. The implications of this research could have applications in technologies as diverse as bullet proof vests, submarine acoustic shielding, airplane radar shielding, earthquake proofing, wind power, and high-speed computing. Nature continually inspires us through its elegant and efficient integration of form and function, and even after 100 years since its discovery, the microtubule is no different.

BIBLIOGRAPHY

[1] J. Löwe, H. Li, K. H. Downing, and E. Nogales. Refined structure of -tubulin at 3.5 resolution11edited by i. a. wilson. *Journal of Molecular Biology*, 313(5):1045 – 1057, 2001.

[2] A. Desai and T. J. Mitchison. Microtubule Polymerization Dynamics. *Annual Review of Cell and Developmental Biology*, 13(1):83–117, 1997.

[3] B. A. Weaver. How taxol/paclitaxel kills cancer cells. *Molecular Biology of the Cell*, 25(18):26772681, 2014.

[4] R. C. Donehower, E. K. Rowinsky, L. B. Grochow, S.M. Longnecker, and D.S. Ettinger. Phase i trial of taxol in patients with advanced cancer. *Cancer treatment reports*, 71(12):11711177, December 1987.

[5] P. B. Schiff and S. B. Horwitz. Taxol stabilizes microtubules in mouse fibroblast cells. *Proceedings of the National Academy of Sciences*, 77(3):15611565, Jan 1980.

[6] M. A. Jordan and L. Wilson. Microtubules and actin filaments: Dynamic targets for cancer chemotherapy. *Current Opinion in Cell Biology*, 10(1):123–130, 1998.

[7] M. Kavallaris, D. Y. Kuo, C. A. Burkhart, D. L. Regl, M. D. Norris, M. Haber, and S. B. Horwitz. Taxol-resistant epithelial ovarian tumors are associated with altered expression of specific beta-tubulin isotypes. *Journal of Clinical Investigation*, 100(5):1282–1293, 1997.

[8] J. F. Diaz and J. M. Andreu. Assembly of purified gdp-tubulin into microtubules induced by taxol and taxotere: Reversibility, ligand stoichiometry, and competition. *Biochemistry*, 32(11):27472755, 1993.

[9] J. Parness and S. B. Horwitz. Taxol binds to polymerized tubulin in vitro . *Journal of Cell Biology*, 91(2):479–487, 11 1981.

[10] J. J. Manfredi, J. Parness, and S. B. Horwitz. Taxol binds to cellular microtubules. *Journal of Cell Biology*, 94(3):688–696, 09 1982.

[11] W. B. Derry, L. Wilson, I. A. Khan, Richard F. Ludueña, and M. A. Jordan. Taxol differentially modulates the dynamics of microtubules assembled from unfractionated and purified ??-tubulin isotypes. *Biochemistry*, 36(12):3554–3562, 1997.

[12] M. A. Jordan, R. J. Toso, D. Thrower, and L. Wilson. Mechanism of mitotic block and inhibition of cell proliferation by taxol at low concentrations. *Proceedings of the National Academy of Sciences*, 90(20):95529556, 1993.

[13] W. B. Derry, L. Wilson, and M. A. Jordan. Substoichiometric binding of taxol suppresses microtubule dynamics. *Biochemistry*, 34(7):22032211, 1995.

[14] G. M. Alushin, G. C. Lander, E. H. Kellogg, R. Zhang, D. Baker, and E. Nogales. High-Resolution microtubule structures reveal the structural transitions in $\alpha\beta$-tubulin upon GTP hydrolysis. *Cell*, 157(5):1117–1129, 2014.

[15] C. Dumontet and B. I. Sikic. Mechanisms of action of and resistance to antitubulin agents: Microtubule dynamics, drug transport, and cell death. *Journal of Clinical Oncology*, 17(3):10611061, 1999.

[16] S. Drukman and M. Kavallaris. Microtubule alterations and resistance to tubulin-binding agents (review). *International Journal of Oncology*, Jan 2002.

[17] G. A. Orr, P. Verdier-Pinard, H. McDaid, and S. B. Horwitz. Mechanisms of Taxol resistance related to microtubules. *Oncogene*, 22(47):7280–7295, 2003.

[18] E. Kyu-Ho Han, L. Gehrke, S.K. Tahir, R.B. Credo, S.P. Cherian, H. Sham, S.H. Rosenberg, and S.C. Ng. Corrigendum to modulation of drug resistance by -tubulin in paclitaxel-resistant human lung cancer cell lines [eur. j. cancer 36 (2000) 15651571]. *European Journal of Cancer*, 43(6):1108, 2007.

[19] S. Ohta, K. Nishio, K. Naohiro, T. Ohmori, Y. Funayama, T. Ohira, H. Nakajima, M. Adachi, and N. Saijo. Characterization of a taxolresistant human smallcell lung cancer cell line. *Japanese Journal of Cancer Research*, 85(3):290–297, 1994.

[20] M. Tan, T. Jing, K. Lan, C. L. Neal, P Li, S. Lee, D. Fang, Y. Nagata, J. Liu, R. Arlinghaus, M. Hung, and D. Yu. Phosphorylation on tyrosine-15 of p34cdc2 by erbb2 inhibits p34cdc2 activation and is involved in resistance to taxol-induced apoptosis. *Molecular Cell*, 9(5):993 – 1004, 2002.

[21] S. Ranganathan, C. A. Benetatos, P. J Colarusso, D. W. Dexter, , and G. R. Hudes. Altered -tubulin isotype expression in paclitaxel-resistant human prostate carcinoma cells. *British Journal of Cancer*, 77(4):562566, 1998.

[22] P. Giannakakou, D. L. Sackett, Y. Kang, Z. Zhan, J. T. M. Buters, T. Fojo, and M. S. Poruchynsky. Paclitaxel-resistant human ovarian cancer cells have mutant -tubulins that exhibit impaired paclitaxel-driven polymerization. *Journal of Biological Chemistry*, 272(27):1711817125, Apr 1997.

[23] C. Dumontet, J. P. Jaffrezou, E. Tsuchiya, G. E. Duran, K. G. Chen, W. B. Derry, L. Wilson, M. A. Jordan, and B. Sikic. Resistance to microtubule-targeted cytotoxins in a k562 leukemia cell variant associated with altered tubulin expression and polymerization. *Bulletin du cancer*, 91 5:E81–112, 2004.

[24] R. B. Montgomery, J. Guzman, D. M. Orourke, and W. L. Stahl. Expression of oncogenic epidermal growth factor receptor family kinases induces paclitaxel

resistance and alters -tubulin isotype expression. *Journal of Biological Chemistry*, 275(23):1735817363, Mar 2000.

[25] G. Carles, D. Braguer, C. Dumontet, V. Bourgarel, A. Gonalves, M. Sarrazin, J. B. Rognoni, and C. Briand. Differentiation of human colon cancer cells changes the expression of -tubulin isotypes and maps. *British Journal of Cancer*, 80(8):11621168, 1999.

[26] M. I. Nicoletti, G. Valoti, P. Giannakakou, Z. Zhan, J. H. Kim, V. Lucchini, F. Landoni, J. G. Mayo, R. Giavazzi, and T. Fojo. Expression of -tubulin isotypes in human ovarian carcinoma xenografts and in a sub-panel of human cancer cell lines from the nci-anticancer drug screen: Correlation with sensitivity to microtubule active agents. *Clinical Cancer Research*, 7(9):2912–2922, 2001.

[27] K. F. Sullivan and D. W. Cleveland. Identification of conserved isotype-defining variable region sequences for four vertebrate beta tubulin polypeptide classes. *Proceedings of the National Academy of Sciences*, 83(12):43274331, Jan 1986.

[28] K. F. Sullivan. Structure and utilization of tubulin isotypes. *Annual Review of Cell Biology*, 4(1):687716, 1988.

[29] A. Banerjee, M. C. Roach, K. A. Wall, M. A. Lopata, D. W. Cleveland, and R. F. Ludueña. A monoclonal antibody against the type ii isotype of beta-tubulin. preparation of isotypically altered tubulin. *Journal of Biological Chemistry*, 263(6):3029–3034, 1988.

[30] M. C. Roach, V. L. Boucher, C. Walss, P. M. Ravdin, and R. F. Luduea. Preparation of a monoclonal antibody specific for the class i isotype of -tubulin: The isotypes of tubulin differ in their cellular distributions within human tissues. *Cell Motility and the Cytoskeleton*, 39(4):273285, 1998.

[31] A. Davis, S. Martinez, D. Nelson, and K. Middleton. A tubulin polymerization microassay used to compare ligand efficacy. *Methods in Cell Biology Microtubules, in vitro*, page 331351, 2010.

[32] M. S. Feizabadi and B. Rosario. Mcf7 microtubules: Cancer microtubules with relatively slow and stable dynamic in vitro. *Biochemical and Biophysical Research Communications*, 484(2):354 – 357, 2017.

[33] D. Panda, H. P. Miller, A. Banerjee, R. F. Ludueña, and L. Wilson. Microtubule dynamics in vitro are regulated by the tubulin isotype composition. *Proceedings of the National Academy of Sciences of the United States of America*, 91(24):11358–11362, 1994.

[34] F. Gittes, B. Mickey, J. Nettleton, and J. Howard. Flexural rigidity of microtubules and actin filaments measured from thermal fluctuations in shape. *Journal of Cell Biology*, 120(4):923–934, 1993.

[35] T. Hawkins, M. Mirigian, J. Li, M. Yasar, D. Sackett, D. Sept, and J. Ross. Perturbations in microtubule mechanics from tubulin preparation. *Cellular and Molecular Bioengineering*, 5, 06 2012.

[36] L. Mahadevan and T. J. Mitchison. Cell biology: Powerful curves. *Nature*, 435(7044):895–897, 2005.

[37] E. Prodan and C. Prodan. Topological phonon modes and their role in dynamic instability of microtubules. *Physical Review Letters*, 103(24):1–4, 2009.

[38] D. Kaya, N. L. Green, C. E. Maloney, and M. F. Islam. Normal Modes and Density of States of Disordered Colloidal Solids. *Science*, 329(5992):656–658, 2010.

[39] C. Gell, V. Bormuth, G. J. Brouhard, D. N. Cohen, S. Diez, C. T. Friel, J. Helenius, B. Nitzsche, H. Petzold, J. Ribbe, E. Schäffer, J. H. Stear, A. Trushko, V. Varga, P. O. Widlund, M. Zanic, and J. Howard. *Microtubule dynamics reconstituted in vitro and imaged by single-molecule fluorescence microscopy*, volume 2. Elsevier, first edit edition, 2010.

[40] M. B. Smith, H. Li, T. Shen, X. Huang, E. Yusuf, and D. Vavylonis. Segmentation and tracking of cytoskeletal filaments using open active contours. *Cytoskeleton*, 67(11):693–705, 2010.

[41] O. Kučera, D. Havelka, and M. Cifra. Vibrations of microtubules: Physics that has not met biology yet. *Wave Motion*, 72(7):13–22, 2017.

[42] S. E. Shirmovsky and D. V. Shulga. Elastic, dipoledipole interaction and viscosity impact on vibrational properties of anisotropic hexagonal microtubule lattice. *BioSystems*, 166:1–18, 2018.

[43] Y. M. Sirenko, M A. Stroscio, and K. W. Kim. Elastic vibrations of microtubules in a fluid. *Physical Review E - Statistical Physics, Plasmas, Fluids, and Related Interdisciplinary Topics*, 53(1):1003–1010, 1996.

[44] S. Portet, J. A. Tuszyński, C. W.V. Hogue, and J. M. Dixon. Elastic vibrations in seamless microtubules. *European Biophysics Journal*, 34(7):912–920, 2005.

[45] A. T. Atanasov. Calculation of vibration modes of mechanical waves on microtubules presented like strings and bars. *American Journal of Modern Physics*, 3:1–11, 2014.

[46] V. Barsegov, J. L. Ross, and R.I. Dima. Dynamics of microtubules: highlights of recent computational and experimental investigations. *Journal of Physics: Condensed Matter*, 29(43):433003, 2017.

[47] A. Ghosh, V. K. Chikkadi, P. Schall, J. Kurchan, and D. Bonn. Density states of colloidal glasses. *Physical Review Letters*, 104:248503, 2010.

[48] J. T. Huzil, K. Chen, L. Kurgan, and J. A. Tuszynski. The roles of β-tubulin mutations and isotype expression in acquired drug resistance. *Cancer Informatics*, 3:117693510700300, 2007.

[49] J Torin Huzil, Richard F Ludueña, and Jack Tuszynski. Comparative modelling of human β tubulin isotypes and implications for drug binding. *Nanotechnology*, 17(4):S90–S100, feb 2006.

[50] D. Sekulic and M. Sataric. An improved nanoscale transmission line model of microtubule: The effect of nonlinearity on the propagation of electrical signals. *Facta universitatis - series: Electronics and Energetics*, 28:133–142, 01 2015.

[51] I. Minoura and E. Muto. Dielectric measurement of individual microtubules using the electroorientation method. *Biophysical Journal*, 90(10):37393748, 2006.

[52] J.A. Tuszynski, D. Friesen, H. Freedman, and et al. Microtubules as sub-cellular memristors. *Scientific Reports*, 10:2108, 2020.

[53] Vladimir G. Kutchoukov, Frederic Laugere, Wim Van Der Vlist, Lukasz Pakula, Yuval Garini, and Andre Bossche. Fabrication of nanofluidic devices using glass-to-glass anodic bonding. *Sensors and Actuators, A: Physical*, 114(2-3):521–527, 2004.

[54] C. Iliescu, H. Taylor, M. Avram, J. Miao, and S. Franssila. A practical guide for the fabrication of microfluidic devices using glass and silicon. *Biomicrofluidics*, 6(1):1–16, 2012.

[55] D. M. Cannon, B. R. Flachsbart, M. A. Shannon, J. V. Sweedler, and P. W. Bohn. Fabrication of single nanofluidic channels in poly(methylmethacrylate) films via focused-ion beam milling for use as molecular gates. *Applied Physics Letters*, 85(7):12411243, 2004.

[56] Q. Xia, K. J. Morton, R. H. Austin, and S. Y. Chou. Sub-10 nm self-enclosed self-limited nanofluidic channel arrays. *Nano Letters*, 8(11):38303833, Dec 2008.

[57] W. Reisner, J. N. Pedersen, and R. H. Austin. Dna confinement in nanochannels: physics and biological applications. *Reports on Progress in Physics*, 75(10):106601, 2012.

[58] N. Kaji, Y. Tezuka, Y. Takamura, M. Ueda, T. Nishimoto, H. Nakanishi, Y. Horiike, and Y. Baba. Separation of Long DNA Molecules by Quartz Nanopillar Chips under a Direct Current Electric Field. *Analytical Chemistry*, 76(1):15–22, 2004.

[59] Y. M. Wang, J. O. Tegenfeldt, W. Reisner, R. Riehn, X. J. Guan, L. Guo, I. Golding, E. C. Cox, J. Sturm, and R. H. Austin. Single-molecule studies of repressor-DNA interactions show long-range interactions. *Proceedings of the National Academy of Sciences of the United States of America*, 102(28):9796–9801, 2005.

[60] M. Lake, C. Narciso, K. Cowdrick, T. Storey, S. Zhang, J. Zartman, and D. Hoelzle. Microfluidic device design, fabrication, and testing protocols. *Protocol Exchange*, Jul 2015.

[61] G. A. C. M. Spierings, J. Haisma, and T. M. Michelsen. Surface-related phenomena in the direct bonding of silicon and fused-silica wafer pairs. *Philips Journal of Research*, 49(1-2):47–63, 1995.

[62] P. Rangsten. Quartz-to-quartz direct bonding. *Journal of The Electrochemical Society*, 146(3):1104, 1999.

[63] J. O. Tegenfeldt, C. Prinz, H. Cao, S. Chou, W. W. Reisner, R. Riehn, Y. M. Wang, E. C. Cox, J. C. Sturm, P. Silberzan, and et al. The dynamics of genomic-length dna molecules in 100-nm channels. *Proceedings of the National Academy of Sciences*, 101(30):1097910983, 2004.

[64] P. Mao. Fabrication and Characterization of Nanofluidic Channels for Studying Molecular Dynamics in Confined Environments Signature of Author Fabrication and Characterization of Nanofluidic Channels for Studying Molecular Dynamics in Confined Environments. *MIT Libraries*, page 95, 2005.

[65] M. Eichler, B. Michel, P. Hennecke, M. Gabriel, and C. Klages. Low-temperature direct bonding of borosilicate, fused silica, and functional coatings. *ECS Transactions*, 33(4):339–348, 2010.

[66] G. Kalkowski, U. Zeitner, T. Benkenstein, J. Fuchs, C. Rothhardt, and R. Eberhardt. Direct wafer bonding for encapsulation of fused silica optical gratings. *Microelectronic Engineering*, 97:177180, 2012.

[67] L. D. Menard and J. M. Ramsey. Fabrication of sub-5 nm nanochannels in insulating substrates using focused ion beam milling. *Nano Letters*, 11(2):512517, Sep 2011.

[68] W. J. Moberlychan, D. P. Adams, M. J. Aziz, G. Hobler, and T. Schenkel. Fundamentals of focused ion beam nanostructural processing: Below, at, and above the surface. *MRS Bulletin*, 32(5):424432, 2007.

[69] H. Y. Wang, R. S. Foote, S. C. Jacobson, J. H. Schneibel, and J. M. Ramsey. Low temperature bonding for microfabrication of chemical analysis devices. *Sensors and Actuators B: Chemical*, 45(3):199207, 1997.

[70] J. Khandurina, T. E. Mcknight, S. C. Jacobson, L. C. Waters, R. S. Foote, and J. M. Ramsey. Integrated system for rapid pcr-based dna analysis in microfluidic devices. *Analytical Chemistry*, 72(13):29953000, 2000.